Islamic University of Gaza
Deanery of Higher Studies
Faculty of Science
Department of Physics

NEW SLAB WAVEGUIDE STRUCTURES
AS OPTICAL SENSORS

By

Hani M. Kullab

Supervisors

Dr. Sofyan Taya
Dr. Taher El-Agez

Submitted to the Faculty of Science as a Partial Fulfillment of the Master of Science (M. Sc.) in Physics

1432 – 2011

To my dear parents for their love, endless support and encouragement.

To my only sister who believed in me, supported me and was always by my side.

To my brothers for their constant support.

To my homeland Palestine the only place in which I feel alive.

Hani M. Kullab

ACKNOWLEDGMENTS

ABSTRACT

This work concerns planar optical waveguide sensors with the focus on slab waveguide structures comprising left-handed materials with simultaneously negative electric permittivity and magnetic permeability. In the last two decades planar waveguides have been introduced in the literature in optical sensing as a novel non-communication application of slab waveguides. Slab waveguide sensors have received an increasing interest due to their immunity to electromagnetic interference, have no danger of ignition, are field resistant, small sized, safe when used in aggressive environments, and mechanically stable.

In this work, a three layer slab waveguide with a left-handed material guiding layer will be studied for sensing applications. TE and TM polarization will be presented. The dispersion relation of the proposed sensor will be obtained. The sensitivity of the sensor to changes in the cladding refractive index and the power flowing through each layer will be presented. The power confinement factor within each layer will also be considered. Moreover, the penetration depth and the Goos-Hanchen shift will be investigated.

Metal-clad planar waveguide sensor with one of the layers is made of left-handed material will be analyzed. Metal-clad waveguide can be operated in two different reflection modes, dip and peak types. Our study will focus on dip type mode.

ملخص البحث

في العقدين الأخيرين، تزايد اهتمام الباحثين بدراسة مرشدات الموجات كمجسات تستخدم في العديد من المجالات مثل المجالات الحيوية والكيميائية والكيميائية الحيوية. وتمتاز هذه المجسات بأنها آمنة غير قابلة للإشتعال، لا تتأثر بالمجال الكهرومغناطيسي المحيط بالإضافة الى حجمها الصغير.

تناقش هذه الأطروحة استخدام مرشدات الموجات الضوئية كمجس والتي تشتمل على طبقة موجهة مكونة من مادة تتمتع بسماحية كهربائية سالبة ونفاذية مغناطيسية سالبة.

في الفصلين الثاني والثالث اشتملت الدراسة على مرشد موجة يتكون من ثلاث طبقات وكانت الطبقة الموجهة تتكون من مادة معامل انكسارها سالب. واقتصرت الدراسة على حالتين من حالات استقطاب المجال الكهرومغناطيسي هما المجال الكهربي المستعرض (TE-modes) والمجال المغناطيسي المستعرض (TM-modes).

لكل حالة من من الحالات السابقة تم اشتقاق علاقة التشتت والحساسية للمجس بالإضافة للطاقة المتدفقة في كل طبقة من طبقات المجس.

في الفصل الرابع تمت دراسة نوع اخر من المرشدات الموجية والتي تشتمل على اربع طبقات ويطلق عليها اسم Metal-clad waveguide بحيث كانت الطبقة الموجهة فيها عبارة عن مادة معامل انكسارها سالب. وتناولت الدراسة طريقة اخرى في تحديد التغيرات الحاصلة في معامل انكسار الوسط المحيط عن طريق دراسة تغير شدة الانعكاس مع زاوية سقوط الشعاع. واشتملت الدراسة على مقارنة هذا المجس مع تراكيب اخرى تدعى Surface plasmon resonance والتي يستخدم فيها نفس الطريقة في الاحساس بالتغيرات الحاصلة في معامل انكسار الوسط المحيط.

وقد وجدت الدراسة ان استخدام المواد سالبة معامل الانكسار كطبقة موجهة يؤدي الى زيادة الحساسية بدرجة عالية مقارنة بالمجسات العادية التي تحتوي على طبقة موجهة مصنوعة من مواد معامل انكسارها موجب.

Publications:

1- Sofyan A. Taya, Taher M. El-Agez, **Hani M. Kullab**, Mazen M. Abadla, and Mohamed M. Shabat, "Theoretical study of slab waveguide optical sensor with left handed material as a core layer", Optica applicata, (in press).

2- Taher M. El-Agez, Sofyan A. Taya, Mohamed M. Shabat, and **Hani M. Kullab**, "Planar waveguide with left-handed material guiding film for refractometry applications", International Journal of Electronics and Communications, (in submission).

List of Figure Captions

CHAPTER THREE

CONTENTS

Chapter one: Foundations for guided-wave optics

Chapter one
Foundations for guided-wave optics

In this chapter, the basic concepts and equations of electromagnetic wave theory required for the comprehension of light wave propagation in optical waveguides are presented, including wave equation, Maxwell's equations, boundary conditions, total internal reflection, and complex Poynting vector. The reflection and transmission of light wave at the interface between two media are investigated. Moreover, a two dimensional slab waveguide is discussed for both TE and TM guided modes.

1.1 Introduction

The fundamentals of optical waveguides are based on the electromagnetic theory of light and its interaction with matter.

In 1845, Michael Faraday observed that a magnetic field would rotate the plane of polarization of light waves passing through the magnetized region. This observation led Faraday to associate light with electromagnetic radiation, but he was unable to quantify this association. He attempted to develop electromagnetic theory by treating the field as lines pointing in the direction of the force that the field would exert on a test charge. James Clerk Maxwell furnished a mathematical framework for Faraday's model in a paper read in 1864 and published a year later. In this paper, Maxwell identified light as "an electromagnetic disturbance in the form of waves propagated through the electromagnetic field according to electromagnetic laws" and demonstrated that the propagation velocity of light was given by the electromagnetic properties of the material.

1.2. Propagation of light

1.2.1. Wave equation

Consider that a one dimensional wave pulse of sinusoidal shape is propagating in the positive x direction, then at t = 0 the wave can be described by the relation:

$$y = f(x,0) = A \sin kx, \qquad (1.1)$$

where the wave amplitude A and the propagation number k are constants that can be varied without changing the harmonic character of the wave.

The propagation number can be defined in terms of the wavelength λ as

$$k = \frac{2\pi}{\lambda} \qquad (1.2)$$
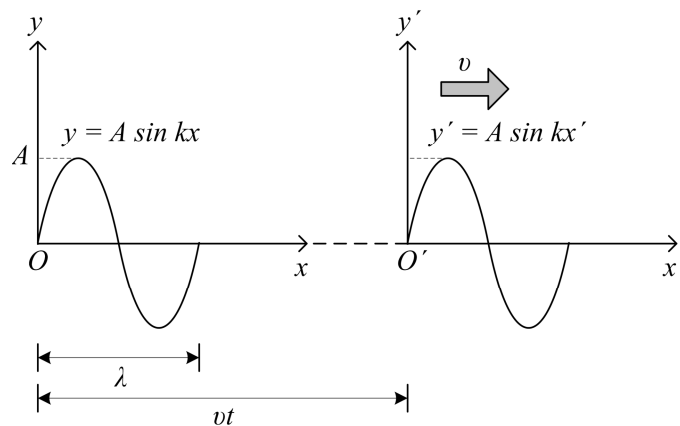
Fig. 1.1 Wave pulse moving at constant speed.

Now, consider the O' system, together with the wave, moves to the right in the positive x-axis with a constant speed υ relative to a fixed coordinate system O, as shown in Fig.1.

In this new coordinate system, the pulse is described by:

$$y' = f(x',0) = A\sin kx'. \tag{1.3}$$

But from Fig.1 we can see that $x' = x - \upsilon t$ and the y-coordinate is identical in either system, $y'=y$, thus Eq. (1.3) now reads:

$$y' = f(x - \upsilon t,0) = A\sin k(x - \upsilon t). \tag{1.4}$$

The periodic time T, the frequency v, and the angular frequency ω are relative to each other through the relations

$$T = \frac{\lambda}{\upsilon}, \tag{1.5}$$

$$v = \frac{1}{T}, \tag{1.6}$$

$$\omega = \frac{2\pi}{T} = 2\pi v. \tag{1.7}$$

Using Euler formula

$$e^{i\theta} = \cos\theta + i\sin\theta, \tag{1.8}$$

it is possible to express a harmonic wave such as

$$y = f(x,t) = Ae^{i(kx-\omega t)}. \tag{1.9}$$

In general, the harmonic wave propagating along any direction in space can be expressed by the wave displacement ψ such that

$$\psi(\mathbf{r},t) = Ae^{i(\mathbf{k}\cdot\mathbf{r}-\omega t+\delta)}, \tag{1.10}$$

where δ is the initial phase.

Now, we wish to derive the wave equation in one dimension. Using chain rule, the space derivative of Eq. (1.1) is given by

$$\frac{\partial y}{\partial x} = \frac{\partial f(x)}{\partial x'}\frac{\partial x'}{\partial x} = \frac{\partial f(x)}{\partial x'}, \tag{1.11}$$

where

$$\frac{\partial x'}{\partial x} = \frac{\partial}{\partial x}(x-\upsilon t)=1. \tag{1.12}$$

Differentiate Eq. (1.11) with respect to space, we get

$$\frac{\partial^2 y}{\partial x^2} = \frac{\partial}{\partial x}\left(\frac{\partial y}{\partial x}\right) = \frac{\partial(\partial y/\partial x)}{\partial x'}\frac{\partial x'}{\partial x} = \frac{\partial}{\partial x'}\left(\frac{\partial f(x)}{\partial x'}\right) = \frac{\partial^2 f(x)}{\partial x'^2}. \tag{1.13}$$

Now, the time derivatives of Eq. (1.1)

$$\frac{\partial y}{\partial t} = \frac{\partial f(x)}{\partial x'}\frac{\partial x'}{\partial t} = -\upsilon\frac{\partial f(x)}{\partial x'}, \tag{1.14}$$

$$\frac{\partial^2 y}{\partial t^2} = \frac{\partial}{\partial t}\left(\frac{\partial y}{\partial t}\right) = \frac{\partial(\partial y/\partial t)}{\partial x'}\frac{\partial x'}{\partial t} = \frac{\partial}{\partial x'}\left(-\upsilon\frac{\partial f(x)}{\partial x'}\right)(-\upsilon) = \upsilon^2\frac{\partial^2 f(x)}{\partial x'^2}. \tag{1.15}$$

Combining Eq. (1.13) and Eq. (1.15), we obtain the relation [1-2]

$$\frac{\partial^2 y}{\partial x^2} = \frac{1}{\upsilon^2}\frac{\partial^2 y}{\partial t^2}. \tag{1.16}$$

Which represents the wave equation of a wave in the form of Eq. (1.1) propagating in one dimension.

In general, the homogeneous wave equation of any harmonic wave propagating along any direction in space can be expressed by [1-15]

$$\nabla^2 \psi = \frac{1}{\upsilon^2} \frac{\partial^2 \psi}{\partial t^2} \, . \tag{1.17}$$

Substituting from Eq. (1.10) into Eq. (1.17) and using the relation

$$\frac{1}{\upsilon^2} = \frac{n^2}{c^2} = \varepsilon\mu \, , \tag{1.18}$$

we get

$$\nabla^2 \psi + \omega^2 \varepsilon\mu\psi = 0 \, , \tag{1.19}$$

where n is the refractive index, ε is the electric permittivity, and μ is the magnetic permeability.

1.2.2. Maxwell's equations and electromagnetic waves

Maxwell's equations for linear and isotropic dielectric materials are given by [1-15]

$$\nabla \times \boldsymbol{E} = -\mu \frac{\partial \boldsymbol{H}}{\partial t} \, , \tag{1.20}$$

$$\nabla \times \boldsymbol{H} = \varepsilon \frac{\partial \boldsymbol{E}}{\partial t} \, , \tag{1.21}$$

$$\nabla \cdot \boldsymbol{E} = 0 \, , \tag{1.22}$$

$$\nabla \cdot \boldsymbol{H} = 0 \, , \tag{1.23}$$

5

where **E**, **H**, *ε, and μ* are the electric field intensity, magnetic field intensity, medium permittivity, and medium permeability, respectively.

Consider an electromagnetic wave, having an angular frequency ω, is propagating in an arbitrary direction in free space with propagation vector **k**. The electric and magnetic fields can be described by the harmonic wave equation in the form of equation (1.10) with the solution

$$E = E_0 \, e^{i(k \cdot r - \omega t)} , \tag{1.24}$$

$$H = H_0 \, e^{i(k \cdot r - \omega t)} . \tag{1.25}$$

By using Eq. (1.24) and Eq. (1.25), Maxwell's equations takes the following form for plane harmonic waves

$$k \times E = \mu \omega \, H , \tag{1.26}$$

$$k \times H = -\varepsilon \omega \, E , \tag{1.27}$$

$$k \cdot E = 0 , \tag{1.28}$$

$$k \cdot H = 0 . \tag{1.29}$$

From equations (1.26-1.29), it is clear that the harmonic variation of the electric and magnetic fields are perpendicular to one another and to the direction of propagation given by $\hat{k}$ as shown in Fig. 1.2.
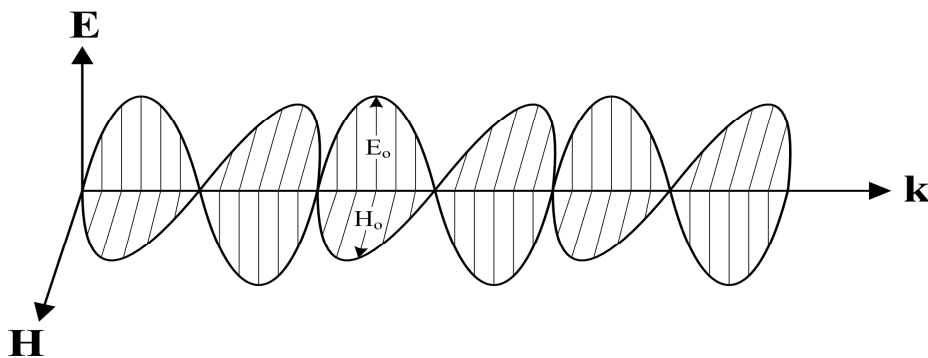
Fig 1.2 Propagation of an electromagnetic wave.

The magnitudes of the fields are related according to the relations

$$H = \frac{\omega}{k} \varepsilon E = \upsilon \varepsilon E ,$$ (1.30)

where $\upsilon = \frac{\omega}{k}$, represents the phase velocity of the wave. Moreover, in terms of the refractive index, $n = \frac{c}{\upsilon}$, equation (1.30) now reads [15]

$$H = \frac{n}{\eta_0} E ,$$ (1.31)

where η_0 is the intrinsic impedance of vacuum and given by

$$\eta_0 = \sqrt{\mu_0 / \varepsilon_0} .$$ (1.32)

The time rate of the flow of electromagnetic energy per unit area is given by the vector $\boldsymbol{S}$, called Poynting vector, which points along the direction of propagation of the wave and defined by [8-16]

$$\boldsymbol{S} = \boldsymbol{E} \times \boldsymbol{H} .$$ (1.33)

Both of the direction and the magnitude of the energy flux are determined by the poynting vector $\boldsymbol{S}$.

The complex electric and magnetic fields can be expressed by

$$\boldsymbol{E}(t) = \mathrm{Re}\left\{ \boldsymbol{E_0}\, e^{i(k \cdot r - \omega t)} \right\} = \frac{1}{2} \left\{ \boldsymbol{E_0}\, e^{i(k \cdot r - \omega t)} + \boldsymbol{E_0^*}\, e^{-i(k \cdot r - \omega t)} \right\},$$ (1.34)

$$\boldsymbol{H}(t) = \mathrm{Re}\left\{ \boldsymbol{H_0}\, e^{i(k \cdot r - \omega t)} \right\} = \frac{1}{2} \left\{ \boldsymbol{H_0}\, e^{i(k \cdot r - \omega t)} + \boldsymbol{H_0^*}\, e^{i(k \cdot r - \omega t)} \right\},$$ (1.35)

where * stands for the complex conjugate.

The time average of the poynting vector is given by

$$\langle S \rangle = \langle E \times H \rangle$$

$$= \frac{1}{4} \left\langle \left(E_0\, e^{i(k \cdot r - \omega t)} + E_0^*\, e^{-i(k \cdot r - \omega t)} \right) \times \left(H_0\, e^{i(k \cdot r - \omega t)} + H_0^*\, e^{i(k \cdot r - \omega t)} \right) \right\rangle$$

$$= \frac{1}{4} \left(E_0 \times H_0^* + E_0^* \times H_0 \right) = \frac{1}{2} \mathrm{Re}\left\{ E \times H^* \right\}. \qquad (1.36)$$

Using Eq. (1.26) and Eq. (1.27) into Eq. (1.36) we get the following two relations [13]

$$\langle S \rangle = \frac{1}{2} \frac{k}{\omega\mu} |E_0|^2 \hat{k} \qquad (1.37)$$

and

$$\langle S \rangle = \frac{1}{2} \frac{k}{\omega\varepsilon} |H_0|^2 \hat{k}. \qquad (1.38)$$

8

1.2.3. Refractive index

Light shows a complicated behavior because of either refraction or absorption of light as its wave strikes the interface between two optically different media. These two phenomena can be described by the refractive index, n, and the extinction coefficient, κ, or by the complex refractive index. The refraction of light is a physical phenomenon occurs because the velocity of light change when light moves from medium to another. This refraction of light can be obtained from the refraction index n, which is given by

$$n = \frac{\text{speed of light in vacuum}}{\text{speed of light in a medium}} = \frac{c}{\upsilon} \ . \tag{1.39}$$

From this definition it is obvious that the speed of light becomes slower in a medium have a high n. In other words, the maximum speed of light is detected in vacuum which characterized by unity refractive index. For example, light travels 1.5341 times faster in vacuum than it does in SiO_2 since the refractive index of SiO_2 is 1.5341.

Another commonly used definition of the refractive index is given by the relation

$$n^2 = \varepsilon_r \, \mu_r, \tag{1.40}$$

where ε_r is the relative permittivity of the medium to the permittivity of vacuum $\varepsilon_0 = 8.854 \times 10^{-12}$ (F/m), and μ_r is its relative permeability of the medium to the permeability of vacuum $\mu_0 = 4\pi \times 10^{-7}$ (H/m). At optical frequencies, $\mu_r = 1$ for non-magnetic materials. Therefore, equation (1.40) now reads

$$n^2 = \varepsilon_r \ . \tag{1.41}$$

When there is no absorption of light in medium (such media are called transparent media), by using equation (1.39), we can obtain the propagation number k such as

$$k = \frac{\omega}{\upsilon} = \frac{\omega}{c}n = \frac{2\pi}{\lambda}n, \qquad (1.42)$$

where λ is the free space wavelength.

Now, the electromagnetic wave propagating in a transparent medium can be obtained by substituting Eq. (1.42) into Eq. (1.10)

$$E = E_{t0}e^{i(\omega t - kx + \delta)} = E_{t0}e^{i\left(\omega t - \frac{2\pi n}{\lambda}x + \delta\right)}, \qquad (1.43)$$

where E_{t0} is the amplitude of the wave inside the transparent medium. Figure 1.3 shows the electromagnetic waves travels into a transparent medium.
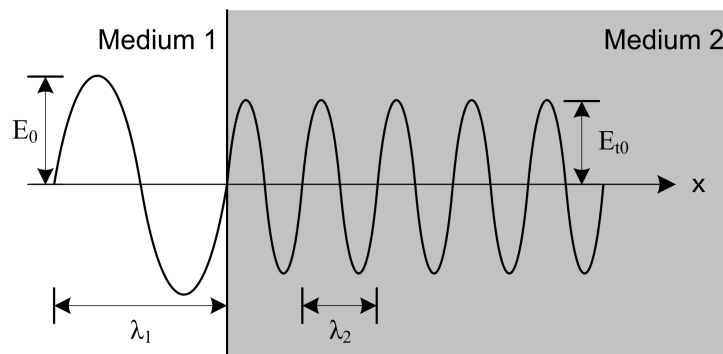
Fig. 1.3 A light wave moves into a transparent medium ($\kappa = 0$).

Figure 1.3 shows that when electromagnetic wave travels from one medium to another, its frequency does not change but its wavelength does. If this is not the case, then energy would be piling up at the boundary. Because there is no mechanism for this to occur, the frequency must be constant [17].

Now using the definition

$$\upsilon = \nu\lambda.$$ (1.44)

Since

$$v_1 = v_2 = v,$$ (1.45)

then

$$\upsilon_1 = \nu\lambda_1,$$ (1.46)

$$\upsilon_2 = \nu\lambda_2.$$ (1.47)

Now dividing Eq.(1.46) by Eq.(1.47) and using $v = c/n$, we get

$$\frac{\lambda_1}{\lambda_2} = \frac{\upsilon_1}{\upsilon_2} = \frac{c/n_1}{c/n_2} = \frac{n_2}{n_1}.$$ (1.48)

Assume that the first medium is vacuum, i.e. $n_1 = 1$, then Eq.(1.48) will be

$$\lambda_2 = \frac{\lambda_1}{n_2}.$$ (1.49)

As mentioned, the propagation of light in a transparent medium determined completely in terms of n. On the other hand, light is almost absorbed in real media, and in this case we need another physical quantity in addition to n to describe the propagation of light in such media. Accordingly, we define the extinction coefficient κ and the complex refractive index N such as [2]

$$N = n - i\kappa.$$ (1.50)

From Eq.(1.41) we can write

$$N^2 = \varepsilon,$$ (1.51)

where ε represents the complex electric permittivity, which is given by

$$\varepsilon = \varepsilon_1 - i\varepsilon_2 . \tag{1.52}$$

From Eqs.(1.50-1.52) we get

$$\varepsilon_1 = n^2 - \kappa^2 \tag{1.53}$$

and

$$\varepsilon_2 = 2n\kappa . \tag{1.54}$$

When there is no light absorption ($\kappa = 0$) then Eq.(1.53) and Eq.(1.54) now read

$$\varepsilon_1 = n^2 , \tag{1.55}$$

$$\varepsilon_2 = 0 . \tag{1.56}$$

In the case of absorbing media, Eq.(1.43) becomes

$$E = E_{t0}e^{i\left(\omega t - \frac{2\pi N}{\lambda}x + \delta\right)} = E_{t0}e^{-\frac{2\pi\kappa}{\lambda}x}e^{i\left(\omega t - \frac{2\pi n}{\lambda}x + \delta\right)} . \tag{1.57}$$

Figure 1.4 illustrate the wave form when light travels into absorbing medium.
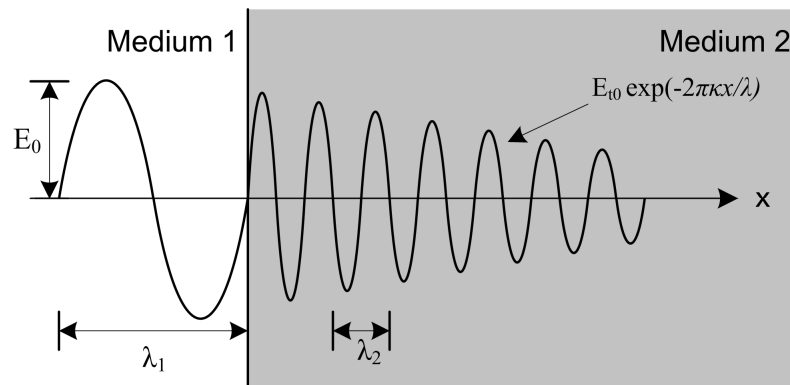
Fig. 1.4 A light wave advances into an absorbing medium ($\kappa > 0$).

1.2.4. Phase and group velocities

Dielectric waveguides are made of dispersive dielectric media, i.e. media whose refractive indices are functions of frequency (wavelength).

Consider two harmonic waves propagating in x direction through a dispersive medium and having the same amplitudes but slightly different angular frequencies. The corresponding propagation constants will, in particular, also differ. The waves are given by

$$\psi_1 = Ae^{i[(k+\Delta k)x-(\omega+\Delta\omega)t]},$$ (1.58)

$$\psi_2 = Ae^{i[(k-\Delta k)x-(\omega-\Delta\omega)t]}.$$ (1.59)

The superposition of the two waves is given by [11,12]

$$\psi_R = Ae^{i[(k+\Delta k)x-(\omega+\Delta\omega)t]} + Ae^{i[(k-\Delta k)x-(\omega-\Delta\omega)t]}.$$ (1.60)

By factoring and collecting terms, Eq.(1.60) now reads

$$\psi_R = Ae^{i(kx-\omega t)}\left[e^{i(x\Delta k-t\Delta\omega)} + e^{-i(x\Delta k-t\Delta\omega)}\right],$$ (1.61)

or

$$\psi_R = 2Ae^{i(kx-\omega t)}\cos(x\Delta k-t\Delta\omega).$$ (1.62)

Eq.(1.62) represents a single wave $2Ae^{i(kx-\omega t)}$, which has a modulation envelope $\cos(x\Delta k-t\Delta\omega)$ as shown in Fig. 1.5. To obtain the phase velocity, υ, of the wave we set the phase of the exponential term to a constant and finding *dx/dt*

$$kx - \omega t = \text{constant},$$

or

$$v = \frac{dx}{dt} = \frac{\omega}{k} \,. \tag{1.63}$$

The modulation envelope travels at a rate $\Delta\omega/\Delta k$, called the *group velocity*, v_g, instead of traveling at a phase velocity, v, of the individual waves. To obtain this group velocity we set the argument of the cosine term equal to a constant and finding *dx/dt*

$$x\Delta k - t\Delta\omega = \text{constant} \,,$$

or

$$v_g = \frac{1}{\Delta k/\Delta\omega} \,. \tag{1.64}$$

In the limit as $\Delta\omega \to 0$

$$v_g = \frac{1}{dk/d\omega} \,. \tag{1.65}$$
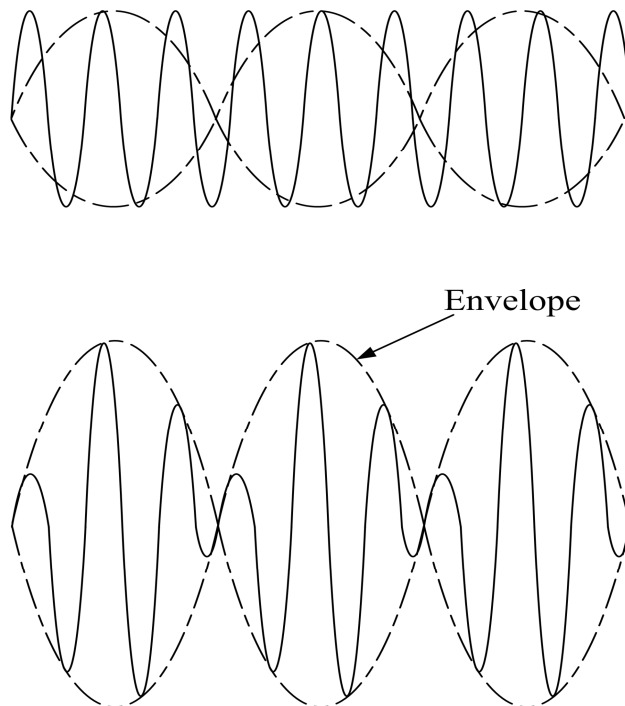
Fig.1.5 Envelope of the combination of two harmonic waves.

In a dispersive medium we can write

$$k = \frac{\omega}{\upsilon} = \frac{\omega}{c} n .$$

(1.66)

Then, Eq.(1.65) becomes

$$\upsilon_g = \frac{1}{\dfrac{d}{d\omega}\left(\dfrac{n\omega}{c}\right)} = \frac{c}{\left(n + \omega\dfrac{dn}{d\omega}\right)} = \frac{c}{n\left(1 + \dfrac{\omega}{n}\dfrac{dn}{d\omega}\right)} = \frac{\upsilon}{\left(1 + \dfrac{\omega}{n}\dfrac{dn}{d\omega}\right)} .$$

(1.67)

In the case of a nondispersive medium, the phase and the group velocity do not differ since the refractive index and the phase velocity are constant. Hence, for free space Eq. (1.67) reads

$$\upsilon_g = \upsilon = c$$

(1.68)

1.2.5. Boundary condition

Consider an electromagnetic wave in the form of equations (1.24) and (1.25) incident from medium 1 into medium 2, as shown in Fig. 1.6. If there is no free charge or free current at the interface, the following boundary conditions must be satisfied at the interface between the two media

1. The tangential components of both E and H are continuous at the boundary [4,15]

$$\hat{n}_1 \times E_1 + \hat{n}_2 \times E_2 = 0, \tag{1.69}$$

$$\hat{n}_1 \times H_1 + \hat{n}_2 \times H_2 = 0, \tag{1.70}$$

where $\hat{n}_i$ is the unit vector normal to the interface between the two media and pointing in the outward direction relative to the region i.

2. The normal components of the electric flux density, D, and the magnetic flux density, B, are continuous at the boundary [4,15]

$$\hat{n}_1 \cdot B_1 + \hat{n}_2 \cdot B_2 = 0, \tag{1.71}$$

$$\hat{n}_1 \cdot D_1 + \hat{n}_2 \cdot D_2 = 0, \tag{1.72}$$

where

$$B = \mu H, \tag{1.73}$$

$$D = \varepsilon E. \tag{1.74}$$

Note that equations (1.73) and (1.74) are called the constitutive relations. By using Eq. (1.69) and Eq. (1.70) we obtain

$$\vec{E}_{1t} = \vec{E}_{2t} \quad \text{and} \quad \vec{H}_{1t} = \vec{H}_{2t}. \tag{1.75}$$

Similarly, from Eq. (1.71) and Eq. (1.72) we get

$$\vec{B}_{1n} = \vec{B}_{2n} \quad \text{and} \quad \vec{D}_{1n} = \vec{D}_{2n}. \tag{1.76}$$

where the subscripts t and n stand for the tangential and normal components, respectively.

At the boundary, the tangential components of the propagation vector must be the same for both media, i.e.:

$$k_{1x} = k_{2x} = k_x. \tag{1.77}$$

From equation (1.42) we can write

$$\frac{n_1^2 \omega^2}{c^2} = k_1^2 = k_x^2 + k_{1z}^2, \tag{1.78}$$

$$\frac{n_2^2 \omega^2}{c^2} = k_2^2 = k_x^2 + k_{2z}^2. \tag{1.79}$$

For the case of plane waves, both components of the wave vector are real. Thus, the angle of incidence θ_1 and the angle of refraction θ_2 can be written as

$$\tan \theta_1 = \frac{k_{1x}}{k_{1z}} = \frac{k_x}{k_{1z}}, \tag{1.80}$$

$$\tan \theta_2 = \frac{k_{2x}}{k_{2z}} = \frac{k_x}{k_{2z}}. \tag{1.81}$$
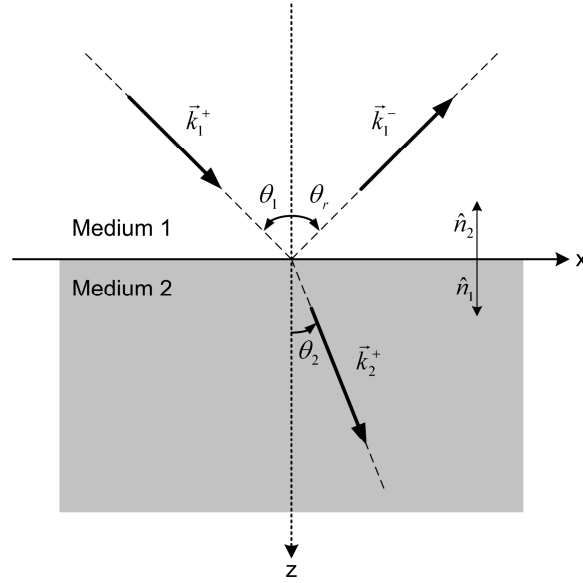
Fig. 1.6. Wave vectors for light incident on the boundary separating two different optical media. The superscripts $^+$ and $^-$ represent a wave propagating downward and upward, respectively.

Now, from Eq. (1.77), we have

$$k_x = k_1 \sin \theta_1 = k_1 \sin \theta_r = k_2 \sin \theta_2 \,. \tag{1.82}$$

Using Eq(1.78) and Eq. (1.79) we get

$$k_x = n_1 \frac{\omega}{c} \sin \theta_1 = n_1 \frac{\omega}{c} \sin \theta_r = n_2 \frac{\omega}{c} \sin \theta_2 \,. \tag{1.83}$$

Equation (1.83) implies that

$$\theta_1 = \theta_r \tag{1.84}$$

and

$$n_1 \sin \theta_1 = n_2 \sin \theta_2 \,. \tag{1.85}$$

Eq. (1.85) is known as *Snell's law.*

1.2.6. Transmission and reflection coefficients

In this subsection, we will discuss the transmission and reflection coefficients at the plane boundary for two different wave polarizations separately. In the first case, the electric fields of the incident waves is orthogonal to the plane of incidence. This case is called the TE-polarization or the perpendicular polarization, it is also referred to as the s-polarized or s-wave. In the second case, the electric fields of the incidence waves is parallel to the plane of incident, this is called TM-polarization (parallel polarization) or p-polarized (p-wave).

I) Perpendicular polarization

The fields components existing for TE-polarization are E_y, H_x, H_z. Figure 1.7 shows reflection and transmission of TE-polarized wave. The boundary conditions state that the electric fields E and magnetic fields H components parallel to an interface are continuous at the boundary

$$E_{1y}^+ + E_{1y}^- = E_{2y}^+. \tag{1.86}$$

Similarly for magnetic fields

$$H_{1x}^+ + H_{1x}^- = H_{2x}^+. \tag{1.87}$$
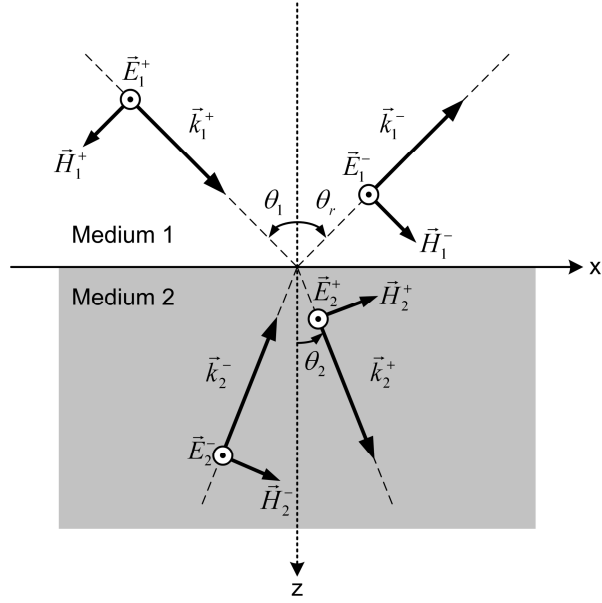
Fig. 1.7 Wave vectors and associated fields for TE polarization.

From Eq. (1.26) we have

$$\boldsymbol{k}_1 \times \boldsymbol{E}_1 = \mu_1 \omega \boldsymbol{H}_1 . \tag{1.88}$$

Equating the x-components we obtain

$$\mu_1 \omega H_{1x}^+ = -k_{1z} E_{1y}^+ , \tag{1.89}$$

$$\mu_1 \omega H_{1x}^- = k_{1z} E_{1y}^- , \tag{1.90}$$

where k_{1z} is the z-component of the wave vector of the wave which propagates downward.

Similarly for the fields in the second medium we have

$$\mu_2 \omega H_{2x}^+ = -k_{2z} E_{2y}^+ . \tag{1.91}$$

Using equations (1.89-1.91), Eq.(1.87) now reads

$$-\frac{k_{1z}}{\mu_1}E_{1y}^+ + \frac{k_{1z}}{\mu_1}E_{1y}^- = -\frac{k_{2z}}{\mu_2}E_{2y}^+ . \tag{1.92}$$

Using Eq.(1.86) and Eq.(1.92), the transmission amplitude of the electric field for TE polarization is given by

$$t_{12_{TE}} = \frac{E_{2y}^+}{E_{1y}^+} = \frac{2}{1+\dfrac{\mu_1}{\mu_2}\dfrac{k_{2z}}{k_{1z}}} = \frac{2\mu_2 k_{1z}}{\mu_2 k_{1z} + \mu_1 k_{2z}} . \tag{1.93}$$

Using equations (1.80) and (1.81) we can write the transmission amplitude in terms of the incidence and transmission angles [11]

$$t_{12_{TE}} = \frac{2}{1+\dfrac{\mu_1}{\mu_2}\dfrac{\tan\theta_1}{\tan\theta_2}} = \frac{2\mu_2 \tan\theta_2}{\mu_2 \tan\theta_2 + \mu_1 \tan\theta_1} . \tag{1.94}$$

The reflection amplitude of the electric field for TE polarization can be obtained from Eq.(1.86) and Eq.(1.92) such as

$$r_{12_{TE}} = \frac{E_1^-}{E_1^+} = \frac{1-\dfrac{\mu_1}{\mu_2}\dfrac{k_{2z}}{k_{1z}}}{1+\dfrac{\mu_1}{\mu_2}\dfrac{k_{2z}}{k_{1z}}} = \frac{\mu_2 k_{1z} - \mu_1 k_{2z}}{\mu_2 k_{1z} + \mu_1 k_{2z}} . \tag{1.95}$$

Similarly, substituting from equations (1.80) and (1.81) into Eq. (1.95) we get [11]

$$r_{12_{TE}} = \frac{1-\dfrac{\mu_1}{\mu_2}\dfrac{\tan\theta_1}{\tan\theta_2}}{1+\dfrac{\mu_1}{\mu_2}\dfrac{\tan\theta_1}{\tan\theta_2}} = \frac{\mu_2 \tan\theta_2 - \mu_1 \tan\theta_1}{\mu_2 \tan\theta_2 + \mu_1 \tan\theta_1} . \tag{1.96}$$

II) Parallel polarization

The field components existing for TM-polarization are H_y, E_x, E_z. Figure 1.8 shows the reflection and transmission of TM-polarized wave. The boundary conditions imply that

$$H_{1y}^+ + H_{1y}^- = H_{2y}^+ . \tag{1.97}$$

Similarly for electric fields

$$E_{1x}^+ + E_{1x}^- = E_{2x}^+ . \tag{1.98}$$
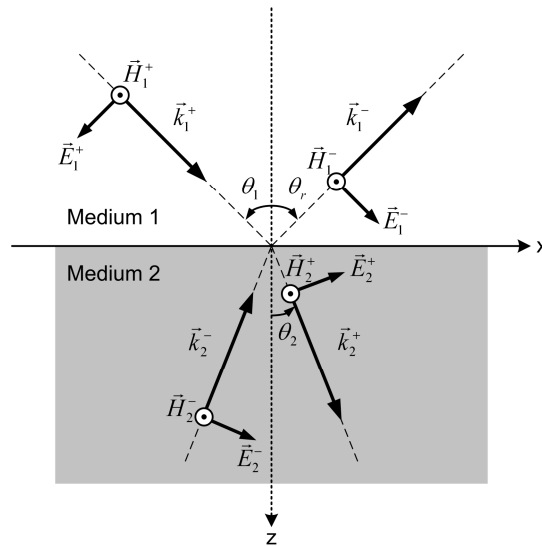
Fig. 1.8 Wave vectors and associated fields for TM polarization.

The transmission and reflection amplitudes for TM-polarization can be obtained if μ_1 and μ_2 in Equations (1.93-1.96) are replaced with ε_1 and ε_2, respectively [11]. Thus

$$t_{12_{TM}} = \frac{2\varepsilon_2 k_{1z}}{\varepsilon_2 k_{1z} + \varepsilon_1 k_{2z}} = \frac{2\varepsilon_2 \tan\theta_2}{\varepsilon_2 \tan\theta_2 + \varepsilon_1 \tan\theta_1} , \tag{1.99}$$

$$r_{12_{TM}} = \frac{\varepsilon_2 k_{1z} - \varepsilon_1 k_{2z}}{\varepsilon_2 k_{1z} + \varepsilon_1 k_{2z}} = \frac{\varepsilon_2 \tan\theta_2 - \varepsilon_1 \tan\theta_1}{\varepsilon_2 \tan\theta_2 + \varepsilon_1 \tan\theta_1} . \tag{1.100}$$

In a multilayer structure as shown in Fig. 1.9., the transmission and reflection coefficients are given by [2]
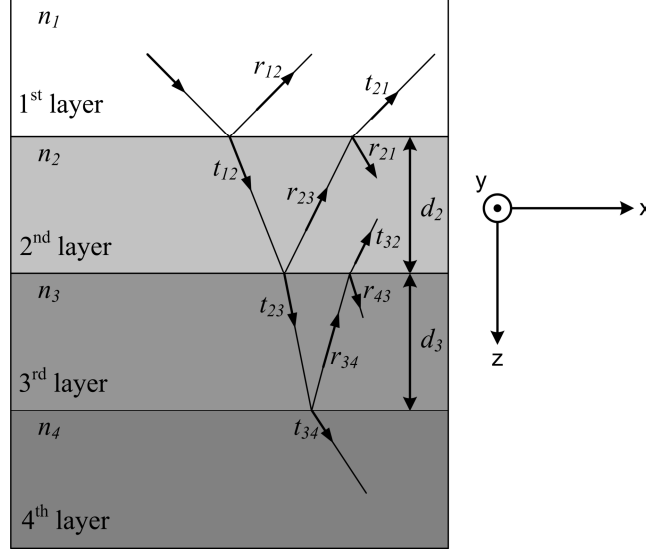
Fig. 1.9. Reflection and transmission in a multilayer structure.

$$r_{123} = \frac{r_{12} + r_{23}\exp(i2k_{2z}d_2)}{1 + r_{12}r_{23}\exp(i2k_{2z}d_2)}, \tag{1.101}$$

$$t_{123} = \frac{t_{12}t_{23}\exp(i2k_{2z}d_2)}{1 + r_{12}r_{23}\exp(i2k_{2z}d_2)}, \tag{1.102}$$

and

$$r_{1234} = \frac{r_{12} + r_{234}\exp(i2k_{3z}d_3)}{1 + r_{12}r_{234}\exp(i2k_{3z}d_3)}, \tag{1.103}$$

$$t_{1234} = \frac{t_{12}t_{234}\exp(i2k_{3z}d_3)}{1 + r_{12}r_{234}\exp(i2k_{3z}d_3)}, \tag{1.104}$$

where k_{jz} is the z-component of wave vector of the wave propagating in j^{th} layer, and d_j is the thickness of the jth layer. The reflectance for TE- and TM-polarized waves are given by [2,6,9,12]

$$R_{TE} = \left|r_{1234_{TE}}\right|^2 \quad \text{and} \quad R_{TM} = \left|r_{1234_{TM}}\right|^2 . \tag{1.105}$$

1.2.7. Total internal reflection

Total internal reflection (TIR) is an optical phenomenon occurs when a light wave is incident at an angle greater than a particular angle, known as a critical angle, from a medium of high refractive index into a medium of lower refractive index.
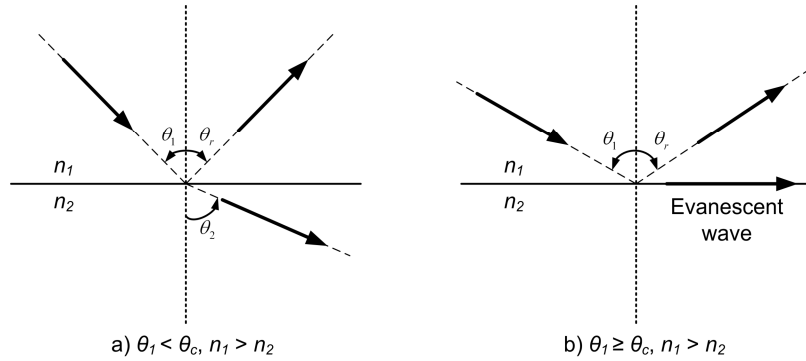
Fig. 1.10. Light reflection at a) $\theta_1 < \theta_c$ and b) $\theta_1 \geq \theta_c$. θ_1 and θ_c represent the incidence and critical angles, respectively.

Figure 1.10(a) shows a ray of light strikes the boundary between two media, when $n_1 > n_2$ this leads to $\theta_1 < \theta_2$. At $\theta_1 = \theta_c$ we observe that $\theta_2 = 90°$. Then, from Snell's law, given by Eq. (1.85), we get the expression of the critical angle [1-15]

$$\theta_c = \arcsin\left(\frac{n_2}{n_1}\right). \qquad (1.106)$$

At $\theta_1 \geq \theta_c$, a so-called an evanescent wave occurs at the boundary as shown in Fig. 1.10(b).

1.3 Planar optical waveguide

1.3.1 Thin film waveguide theory

The simplest optical waveguide structure is a slab structure with a step index profile consisting of three layers, two of which are thick known as the substrate and the cover surrounding a thin layer called the guiding film. To keep the wave guided inside the film layer, the refractive index of the film n_f must be larger than that of the substrate n_s and that of the cover layer n_c. Thus, fields are mainly confined in the film layer. Throughout our discussions, we assume that $n_f > n_s \geq n_c$. If $n_s = n_c$, we have a symmetric waveguide. On the other hand, if $n_s \neq n_c$, the slab waveguide is asymmetric. Figure 1.11 shows a conventional asymmetric slab waveguide with $n_f > n_s > n_c$.

Furthermore, the film thickness d should be comparable to the operating wave length λ. In contrary, the substrate and cover (cladding) layers are much thicker than λ.
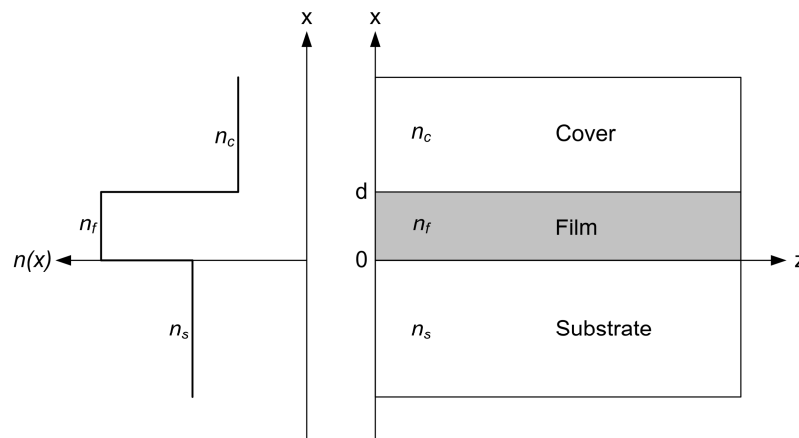
Fig. 1.11. Basic structure and refractive index profile of the optical slab waveguide.

1.3.2. Basic equations

Consider an electromagnetic wave which advances into a waveguide shown in Fig. 1.11 and propagates in the z direction. The electric field and the magnetic field are assumed to have the sinusoidal form

$$E = E_0(x,y)\, e^{i(\omega t - \beta z)}, \tag{1.107}$$

$$H = H_0(x,y)\, e^{i(\omega t - \beta z)}, \tag{1.108}$$

where β represents the longitudinal component of the wave vector. Substituting equations (1.107) and (1.108) into equations (1.20) and (1.21), the following equations are obtained [13-15]

$$\left.\begin{aligned}
\frac{\partial E_z}{\partial y} + i\beta E_y &= -i\omega\mu\, H_x \\[6pt]
i\beta E_x + \frac{\partial E_z}{\partial x} &= i\omega\mu\, H_y \\[6pt]
\frac{\partial E_y}{\partial x} - \frac{\partial E_x}{\partial y} &= -i\omega\mu\, H_z \\[6pt]
\frac{\partial H_z}{\partial y} + i\beta H_y &= i\omega\varepsilon\, E_x \\[6pt]
i\beta H_x + \frac{\partial H_z}{\partial x} &= -i\omega\varepsilon\, E_y \\[6pt]
\frac{\partial H_y}{\partial x} - \frac{\partial H_x}{\partial y} &= i\omega\varepsilon\, E_z
\end{aligned}\right\} \tag{1.109}$$

The waveguide is assumed to be infinitely extended in the y direction. Therefore, there is no variation in the waveguide geometry in the y direction and hence

$$\frac{\partial E_i}{\partial y} = 0\ , \quad \frac{\partial H_i}{\partial y} = 0 \qquad i = x, y, \text{ and } z. \tag{1.110}$$

For nonmagnetic materials $\mu_r = 1$, then $\mu = \mu_0$ and $\varepsilon = \varepsilon_0\, n^2$. Using these relations and Eq. (1.110), the set of equations (1.109) become

$$i\beta E_y = -i\omega\mu_0 H_x, \tag{1.111}$$

$$i\beta E_x + \frac{dE_z}{dx} = i\omega\mu_0 H_y, \tag{1.112}$$

$$\frac{dE_y}{dx} = -i\omega\mu_0 H_z, \tag{1.113}$$

$$i\beta H_y = i\omega\varepsilon_0 n^2 E_x, \tag{1.114}$$

$$i\beta H_x + \frac{dH_z}{dx} = -i\omega\varepsilon_0 n^2 E_y, \tag{1.115}$$

$$\frac{dH_y}{dx} = i\omega\varepsilon_0 n^2 E_z. \tag{1.116}$$

Equations (1.111) through (1.116) are divided into two independent electromagnetic modes, TE mode and TM mode. Equations (1.111), (1.113), and (1.115) involves E_y, H_x, and H_z only, which are the fields of TE mode while equations (1.112), (1.114), and (1.116) involves H_y, E_x, and E_z only, which are the fields of TM mode.

I) Transverse electric modes

Using equations (1.111) and (1.113), the two magnetic field components H_x and H_z of TE mode can be expressed in terms of the electric field component E_y by [13-15]

$$H_x(x) = -\frac{\beta}{\omega\mu_0} E_y(x), \tag{1.117}$$

$$H_z(x) = i\frac{1}{\omega\mu_0}\frac{d}{dx} E_y(x). \tag{1.118}$$

Substituting equations (1.117) and (1.118) into (1.115) gives the wave equation, Helmholtz equation, for TE mode :

$$\frac{d^2}{dx^2}E_y(x)+(k^2n^2-\beta^2)E_y(x)=0 \,.$$
(1.119)

The fields and propagation constant of TE modes can be obtained by solving for $E_y(x)$ in Eq.(1.119) and choosing constants to satisfy the boundary conditions.

II) Transverse magnetic modes

From equations (1.114) and (1.116), the two electric field components E_x and E_z of the TM mode in terms of the magnetic field component H_y can be expressed as [13-15]

$$E_x(x)=\frac{\beta}{\omega\varepsilon_0 n^2}H_y(x) \,,$$
(1.120)

$$E_z(x)=-i\frac{1}{\omega\varepsilon_0 n^2}\frac{d}{dx}H_y(x) \,.$$
(1.121)

Substituting from equations (1.120) and (1.121) into (1.112) yields the wave equation, Helmholtz equation, for TM mode :

$$\frac{d^2}{dx^2}H_y(x)+(k^2n^2-\beta^2)H_y(x)=0$$
(1.122)

Solving for $H_y(x)$ in the above equation, we get the fields and propagation constant of the TM modes.

1.3.3 The propagating power

Using the divergence theorem for a vector $\mathbf{A}$ in an arbitrary volume $\mathbf{V}$, we have

$$\iiint_V (\nabla \cdot A)\, d\tau = \iint_S A \cdot n\, ds, \tag{1.123}$$

where $\mathbf{n}$ represent a unit vector orthogonal to the surface $\mathbf{S}$ enclosing the volume $\mathbf{V}$ and pointing outward. Now, let $A = E \times H$ then Eq. (1.123) will be

$$\iiint_V \nabla \cdot (E \times H)\, d\tau = \iint_S (E \times H) \cdot n\, ds. \tag{1.124}$$

Using the vector identity

$$\nabla \cdot (A \times B) = B \cdot (\nabla \times A) - A \cdot (\nabla \times B), \tag{1.125}$$

then, eq. (1.124) yields

$$\iiint_V (H \cdot (\nabla \times E) - E \cdot (\nabla \times H))\, d\tau = \iint_S (E \times H) \cdot n\, ds. \tag{1.126}$$

Now substituting from Maxwell's equations, Eq. (1.20) and Eq. (1.21), into Eq. (1.126), we obtain

$$\iiint_V (\mu H \cdot \frac{\partial H}{\partial t} + \varepsilon E \cdot \frac{\partial E}{\partial t})\, d\tau = -\iint_S (E \times H) \cdot n\, ds. \tag{1.127}$$

But

$$\mu H \cdot \frac{\partial H}{\partial t} = \frac{\partial}{\partial t} \frac{1}{2} \mu H^2 = \frac{\partial}{\partial t} u_H, \tag{1.128}$$

$$\varepsilon\,\boldsymbol{E}\cdot\frac{\partial\boldsymbol{E}}{\partial t}=\frac{\partial}{\partial t}\frac{1}{2}\varepsilon\,E^{2}=\frac{\partial}{\partial t}u_{E}\,,\qquad(1.129)$$

where u_H and u_E represents the energy density per unit volume associated with the magnetic and electric fields, respectively. The left hand side of Eq. (1.127) represents the rate at which energy is transported by the electromagnetic wave, or the total power flow into the volume V bounded by S. Thus equation (1.127) becomes

$$P=-\iint\limits_{s}(\boldsymbol{E}\times\boldsymbol{H})\cdot\boldsymbol{n}\,ds=\iint\limits_{s}(\boldsymbol{E}\times\boldsymbol{H})\cdot\boldsymbol{u}\,ds=\iint\limits_{s}\boldsymbol{S}\cdot\boldsymbol{u}\,ds\,,\qquad(1.130)$$

where $\boldsymbol{u}$ is a unit vector in opposite direction of $\boldsymbol{n}$.

The time average of the total power flow can be obtained by substituting from Eq. (1.36) into last equation, then

$$P=\iint\limits_{s}\langle\boldsymbol{S}\rangle\cdot\boldsymbol{u}\,ds=\iint\limits_{s}\frac{1}{2}\mathrm{Re}\left\{\boldsymbol{E}\times\boldsymbol{H}^{*}\right\}\cdot\boldsymbol{u}\,ds\,.\qquad(1.131)$$

Substituting from Eq. (1.37) into Eq. (1.131) we get the total power flow for TE-polarization [13-15]

$$P=\frac{1}{2}\frac{k_{x}}{\omega}\iint\limits_{s}\frac{\left|E_{y}(x)\right|^{2}}{\mu(x)}\,dxdy\,.\qquad(1.132)$$

Similarly, substituting from Eq. (1.38) into Eq. (1.134) we get the total power flow for TM-polarization [13-15]

$$P=\frac{1}{2}\frac{k_{x}}{\omega}\iint\limits_{s}\frac{\left|H_{y}(x)\right|^{2}}{\varepsilon(x)}\,dxdy\,.\qquad(1.133)$$

30

1.4. Optical sensing

Optical waveguide sensors have been used for analytical purposes for a number of years [18-22]. The sensing operation of the slab waveguide sensors is performed by the evanescent tail of the modal field in the cover medium. The guided electromagnetic field of the waveguide mode extends as an evanescent field into the cladding and the substrate media and senses an effective refractive index of the guided mode. The effective refractive index of the propagating mode depends on the structure parameters, e.g., the guiding layer thickness and dielectric permittivity and magnetic permeability of the media constituting the waveguide. As a result, any change in the refractive index of the cladding results in a change in the effective refractive index of the guided mode. The basic sensing principle of the planar waveguide sensor is to measure the changes in the effective refractive index due to changes in the refractive index of the cladding [23]. Many theoretical and experimental studies have been conducted to improve the sensitivity of slab waveguide sensors. Taya et al. [24-27] proposed optical waveguide sensors in which one or both of the surrounding media have an intensity dependent refractive index. It is found that utilizing nonlinear media can enhance the sensitivity of slab waveguide sensors. Another class of optical waveguide sensor has been proposed with the so-called reverse symmetry design [28,29]. In these structures the substrate has a refractive index being less than that of the cladding medium. This design offers deeply penetrating evanescent optical fields into the analyzed cover sample. Therefore, the sensitivity has shown an improvement in the reverse symmetry configuration.

The normalized analysis depends on the distribution of the cover medium, if the cover contains a thin layer, known as an adlayer or in some literature affinity layer, at the surface of the sensor, then the sensing operation is called the surface sensing. Otherwise, if the cover medium is homogeneously distributed, the operation is called homogeneous sensing.

In the case of the surface sensing, the sensitivity can be found out by measuring the change of the effective index due to the change of the adlayer width d_A or the refractive index of the adlayer n_A, such as [19,30]

$$S_{d_A} = \frac{\partial N}{\partial d_A}, \qquad S_{n_A} = \frac{\partial N}{\partial n_A} \qquad (1.134)$$

For homogeneous sensing, the cover sensitivity is the change of effective index with respect to the change of cover index [19,30]

$$S_{n_c} = \frac{\partial N}{\partial n_c} \qquad (1.135)$$

1.5 Metamaterials

1.5.1 Concept of metamaterials

In the past few years, new developments in structured electromagnetic materials have given rise to negative refractive index materials which have both negative dielectric permittivity ε and negative magnetic permeability μ in some frequency ranges [31-33].

The origin of the term metamaterial has been attributed to R. Walser who define them as "Macroscopic composites having a manmade, three-dimensional, periodic cellular architecture designed to produce an optimized combination, not available in nature, of two or more responses to specific excitation" [34].

The prefix "meta", in Greek implies "beyond" or "after", as in metaphysics, suggests that it possesses properties that transcend those available in nature [35,36].

The history of these materials began with the paper of Veselago [37], who predicted a number of remarkable properties of waves in a material with simultaneously negative dielectric permittivity ε and magnetic permeability μ. Such materials are usually termed as metamaterials or left-handed materials (LHMs), since the electric and magnetic fields form a left-handed set of vectors with the wave vector and hence the direction of propagation is in the opposite direction of energy flow [35-40].

In addition, there are two mathematical solutions for $n^2 = \mu\varepsilon$ namely $n = \pm\sqrt{\mu\varepsilon}$. In ordinary materials the permittivity and permeability are both positive. Thus it is natural to choose the positive square root $n = \sqrt{\mu\varepsilon}$. When $\varepsilon < 0$ and $\mu < 0$, physical and mathematical considerations lead to choosing the negative square root $n = -\sqrt{\mu\varepsilon}$. For this reason, left-handed materials are also referred to as negative index materials (NIMs). Consequently, when such media are interfaced with conventional dielectrics, Snell's law is reversed, leading to the negative refraction of an incident electromagnetic plane wave. Moreover, the Goos-Hanchen shift, which is the observed displacement from the point of incident during TIR, must be negative since the energy flow and wavefront propagation are antiparallel.

Besides the negative refraction and backward-wave propagation, Veselago also showed some new features like reversed Doppler shift and backward Cerenkov radiation in metamaterials [37,40].

1.5.2 A brief historical review

In 1968, Veselago predicted that substances with negative electric permittivity ε and negative permeability μ have some properties different from those with positive ε and μ [37].

Pendry et al. [41,42] first theoretically suggested and later experimentally demonstrated that a composite medium of periodically placed thin metallic wires can behave as an effective plasma medium for radiation with wavelength much larger than the spatial periodicity of the structure. For frequencies lower than a particular (plasma) frequency, the thin wire structure therefore exhibits a negative permittivity ε.

Smith et al [43] constructed a LHM using the combination of periodic rods and split rings and they performed many experiments in the microwave range to point out that the nature of this material is unlike any existing material. The first experimental investigation of negative index of refraction was achieved by Shelby et al in 2001 [44].

The interaction of electromagnetic waves with stratified isotropic LHMs was investigated by Kong [45]. He investigated the reflection and transmission beams, field solution of guided waves, and linear and dipole antennas in stratified structure of LHMs. The theory of LHMs and their electromagnetic properties, possible future applications, physical remarks, and intuitive justifications are provided by Engheta in 2003 [46].

Chew [47] analyzed the energy conservation property of a LHM and the realistic Sommerfeld problem of a point source over a LHM half space and a LHM slab. In 2006, Sabah et al [48] presented the reflected and transmitted powers due to the interaction of electromagnetic waves with a LHM. They studied the effects of the structure parameters, incidence angle, and the frequency on the reflected and transmitted powers for lossless LHM. The electromagnetic wave propagation through frequency-dispersive and lossy double-negative slab embedded between two different semi-infinite media was presented by Sabah et al [49].

Due to the fabrication technologies, the LHMs are widely used in filters, absorbers, lens, microwave components, and antennas, etc. Furthermore, many researchers continue to study the potential applications of LHMs [50-52].

1.5.3 Uses and applications

Because of the exciting and unusual properties, metamaterials are finding a lot of applications. The most exciting potential application is the perfect lens. Compared to a conventional convex lens, the LHM lens looks quite exotic in that it does not have any axis or curvature, nor does it focus parallel rays or magnify small objects. All of these features were recognized in the seminal paper by Veselago [37]. The other outstanding feature of the metamaterial is superlens [53,54], which is widely used in the super-resolution medical imaging, optical imaging, and nondestructive detections. In 2004, A. Grbic et al. realized the first superlens in the microwave regime [55], which demonstrated resolution three times better than the diffraction limit. Fang et al. proposed the first optical superlens using thin silver film in 2005 [56], which breaks the diffraction limit and produces super-resolution images.

For LHMs, the cloaking devices have gained more attention [57-63]. The successful demonstrations of invisible cloaks experimentally in the microwave regime [57,58] make it possible to realize cloaking devices in the future. With the vast development of metamaterials, more applications will be found in the future.

Chapter two

Slab waveguide optical sensor with left handed material as a core layer: TE-mode

In this chapter, a three-layer planar waveguide consisting of thin left handed material core layer is investigated for sensing applications. The sensitivity of the proposed sensor to the changes in the refractive index of the cladding and the power flowing within each layer will be presented and will be compared to conventional waveguide sensor. Moreover, the power confinement factor in each layer will be obtained.

2.1. Structure analysis

We consider asymmetric slab waveguide with a LHM layer occupying the region $0 < z < d$, which is characterized by an electric permittivity ε_2 and a magnetic permeability μ_2 such that

$$\varepsilon_2(\omega) = 1 - \frac{\omega_p^2}{\omega^2 + i\gamma\omega}, \qquad\qquad (2.1)$$

$$\mu_2(\omega) = 1 - \frac{F\omega^2}{\omega^2 - \omega_o^2 + i\gamma\omega}, \qquad\qquad (2.2)$$

where ω_p is the plasma frequency, ω_o is the resonance frequency, γ is the electron scattering rate, and F is the fractional area of the unit cell occupied by the split ring [64,65]. The slab is sandwiched between a dielectric cladding occupying the region $z > d$ and having ε_3 and μ_3 and a dielectric substrate occupying the region $z < 0$ and having ε_1 and μ_1 as shown in Fig. 2.1.

36
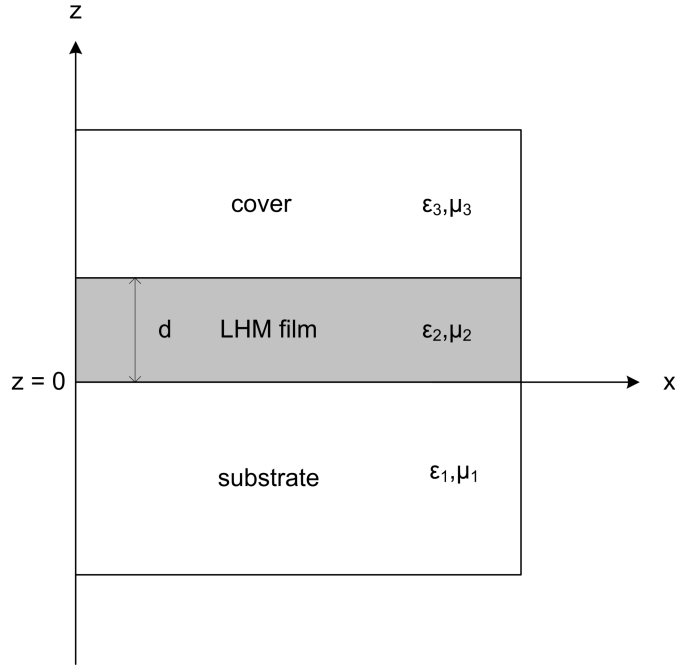
Fig. 2.1. Schematic diagram of a left-handed material slab sandwiched between two semi-infinite media.

2.2. The dispersion equation

In order to obtain the dispersion relation, it is necessary to solve Maxwell's equations for the three-layer structure. The solutions for the time harmonic electric field are given by

$$\vec{E} = \begin{cases} A\,e^{\beta_1 z}\,e^{ik_x x}\,\hat{y} & \text{Substrate region} \\ (B\,e^{ik_{z,2}z} + C\,e^{-ik_{z,2}z})e^{ik_x x}\,\hat{y} & \text{Film region} \\ D\,e^{-\beta_3(z-d)}e^{ik_x x}\,\hat{y} & \text{Cladding region} \end{cases} \tag{2.3}$$

Using equations (1.117) and (1.118) we can find the nonvanishing components of the magnetic field

$$\vec{H} = \begin{cases} \dfrac{A}{\omega\mu_0\mu_1}e^{\beta_1 z}(i\beta_1\,\hat{x} + k_x\,\hat{z})e^{ik_x x} & \text{Substrate region} \\[4mm] \dfrac{1}{\omega\mu_0\mu_2}\left[-Be^{ik_{z,2}z}(k_{z,2}\,\hat{x} - k_x\,\hat{z}) + Ce^{-ik_{z,2}z}(k_{z,2}\,\hat{x} + k_x\,\hat{z})\right]e^{ik_x x} & \text{Film region} \\[4mm] -\dfrac{D}{\omega\mu_0\mu_3}e^{-\beta_3(z-d)}(i\beta_3\,\hat{x} - k_x\,\hat{z})e^{ik_x x} & \text{Cladding region} \end{cases}$$

(2.4)

where $\hat{x}, \hat{y}$ and $\hat{z}$ are the unit vectors in x, y, and z directions, respectively. The constants *A, B, C, D* and the longitudinal propagation constant (k_x) are chosen to satisfy the boundary conditions. The relation between β_j (j=1, 2 and 3) and the normal vector component $k_{z,j}$ is given by

$$\beta_j = -ik_{z,j} = (k_x^2 - \varepsilon_j\mu_j k_0^2)^{1/2},$$

(2.5)

where $k_x = k_0 N$, $k_0 = \dfrac{2\pi}{\lambda}$, λ is the vacuum wavelength of the guided light, and

N is the effective refractive index.

The boundary conditions require that the tangential components of *E* and *H* to be continuous at $z = 0$ and $z = d$, yielding a set of homogeneous linear equations for the coefficients *A, B, C,* and *D*. The determinant of this set must be zero for a nontrivial solution to exist. After some manipulations, the following equation, which is the bulk polariton dispersion relation for TE waves, is obtained

$$\left(\dfrac{k_{z,2}}{\mu_2}\right)^2 - \left(\dfrac{\beta_3}{\mu_3} + \dfrac{\beta_1}{\mu_1}\right)\dfrac{k_{z,2}}{\mu_2}\cot(k_{z,2}d) - \dfrac{\beta_3}{\mu_3}\dfrac{\beta_1}{\mu_1} = 0.$$

(2.6)

The surface wave mode can be obtained with $k_{z,2}$ is replaced by $i\beta_2$. In this case the dispersion relation becomes

$$\left(\dfrac{\beta_2}{\mu_2}\right)^2 + \left(\dfrac{\beta_1}{\mu_1} + \dfrac{\beta_3}{\mu_3}\right)\dfrac{\beta_2}{\mu_2}\coth(\beta_2 d) + \dfrac{\beta_1}{\mu_1}\dfrac{\beta_3}{\mu_3} = 0.$$

(2.7)

2.3. The sensitivity

The sensitivity of the evanescent field sensor is calculated as the change of the effective refractive index with respect to the change of the cladding refractive index (n_3); i.e.,

$$S = \frac{\partial N}{\partial n_3} .$$

(2.8)

Differentiating the dispersion relation given by Eq.(2.6) with respect to N, we get

$$S = \frac{n_3}{N} \frac{\mu_3 k_{z,2}^2}{\beta_3(\mu_2^2 \beta_3^2 + \mu_3^2 k_{z,2}^2)} \left(\frac{d}{\mu_2} + \frac{\mu_1(k_{z,2}^2 + \beta_1^2)}{\beta_1(\mu_2^2 \beta_1^2 + \mu_1^2 k_{z,2}^2)} + \frac{\mu_3(k_{z,2}^2 + \beta_3^2)}{\beta_3(\mu_2^2 \beta_3^2 + \mu_3^2 k_{z,2}^2)} \right)^{-1}$$

(2.9)

For the surface mode, the sensitivity can be obtained by differentiating Eq.(2.7) which gives

$$S = \frac{n_3}{N} \frac{\mu_3 \beta_2^2}{\beta_3(\mu_2^2 \beta_3^2 - \mu_3^2 \beta_2^2)} \left(-\frac{d}{\mu_2} + \frac{\mu_1(\beta_2^2 - \beta_1^2)}{\beta_1(\mu_2^2 \beta_1^2 - \mu_1^2 \beta_2^2)} + \frac{\mu_3(\beta_2^2 - \beta_3^2)}{\beta_3(\mu_2^2 \beta_3^2 - \mu_3^2 \beta_2^2)} \right)^{-1}$$

(2.10)

2.4. Power flowing within the waveguide layers

Due to the close connection between the sensitivity of the slab waveguide sensor and the power flow, it is worth to find the total time-average power transported by the waveguide,

$$P_{total} = \frac{k_x}{2\omega} \int_{-\infty}^{\infty} \frac{|E_y(z)|^2}{\mu_i(z)} dz .$$

(2.11)

Substituting for $E_y(z)$ from Eq.(2.3) into Eq.(2.11), the time-average power flowing in the substrate, the film, and the cladding layers are respectively given by

$$P_1 = \frac{k_x |A|^2}{4\omega\mu_o\mu_1\beta_1}, \tag{2.12}$$

$$P_2 = \frac{k_x}{4\omega\mu_o\mu_2}\left\{\frac{|B|^2}{ik_{z,2}}(e^{2k_{z,2}d}-1)+\frac{|C|^2}{ik_{z,2}}(1-e^{-2k_{z,2}d})+4BCd\right\}, \tag{2.13}$$

$$P_3 = \frac{k_x |D|^2}{4\omega\mu_o\mu_3\beta_3}. \tag{2.14}$$

The coefficients *A*, *B*, *C*, and *D* are related to each other through the equations

$$B = \frac{A}{2}\left(1-i\frac{\mu_2}{\mu_1}\frac{\beta_1}{k_{z,2}}\right), \tag{2.15}$$

$$C = \frac{A}{2}\left(1+i\frac{\mu_2}{\mu_1}\frac{\beta_1}{k_{z,2}}\right), \tag{2.16}$$

$$D = A\left(1-i\frac{\mu_2}{\mu_1}\frac{\beta_1}{k_{z,2}}\right)\left(\frac{\mu_3 k_{z,2}}{\mu_3 k_{z,2}+i\beta_3\mu_2}\right)e^{ik_{z,2}d}. \tag{2.17}$$

It is instructive to study the percentage of time-average power contained in each region. To quantify the fractional power within the jth layer, we define the jth layer confinement factor Γ_j as

$$\Gamma_j = \frac{Time-average\ power\ transported\ in\ the\ j^{th}\ region}{Total\ time-average\ power\ transported\ by\ the\ waveguide}. \tag{2.18}$$

The following relation must hold between the confinement factors

$$\sum_{j=1}^{3} \Gamma_j = 1. \tag{2.19}$$

Thus, the confinement factor of the substrate, film, and cladding are respectively given by

$$\Gamma_s = \cfrac{1/\mu_1\beta_1}{\left[\cfrac{1}{\mu_1\beta_1} + \cfrac{i}{4\mu_2 k_{z,2}}\left(b_-^2 a_+ - b_+^2 a_- - 4ik_{z,2}db_-b_+\right) - \cfrac{\mu_3 k_{z,2}^2 b_-^2}{\beta_3(\mu_2\beta_3 - i\mu_3 k_{z,2})^2}e^{2ik_{z,2}d}\right]}$$

(2.20)

$$\Gamma_f = \cfrac{\cfrac{i}{8\mu_2 k_{z,2}}\left(b_-^2 a_+ - b_+^2 a_- - 4ik_{z,2}db_-b_+\right)}{\left[\cfrac{1}{2\mu_1\beta_1} + \cfrac{i}{8\mu_2 k_{z,2}}\left(b_-^2 a_+ - b_+^2 a_- - 4ik_{z,2}db_-b_+\right) - \cfrac{\mu_3 k_{z,2}^2 b_-^2}{2\beta_3(\mu_2\beta_3 - i\mu_3 k_{z,2})^2}e^{2ik_{z,2}d}\right]}$$

(2.21)

$$\Gamma_c = \cfrac{-4\cfrac{\mu_3 k_{z,2}^2 b_-^2}{\beta_3(\mu_2\beta_3 - i\mu_3 k_{z,2})^2}e^{2ik_{z,2}d}}{\left[\cfrac{1}{\mu_1\beta_1} + \cfrac{i}{4\mu_2 k_{z,2}}\left(b_-^2 a_+ - b_+^2 a_- - 4ik_{z,2}db_-b_+\right) - \cfrac{\mu_3 k_{z,2}^2 b_-^2}{\beta_3(\mu_2\beta_3 - i\mu_3 k_{z,2})^2}e^{2ik_{z,2}d}\right]}$$

(2.22)

where

$$b_\pm = \left(1 \pm i\frac{\mu_2}{\mu_1}\frac{\beta_1}{k_{z,2}}\right), \tag{2.23}$$

$$a_\pm = 1 - e^{\pm 2ik_{z,2}d}. \tag{2.24}$$

2.5. Penetration depth and Goos-Hanchen shift

The effective guide thickness is an important factor in the dispersion of the effective refractive index and in the application of optical sensing. Foreknowing this, we calculate the effective guide thickness from the ray

penetrations at the upper and lower boundaries of the guiding layer. The penetration of the guided wave from the guiding layer into the surrounding media can be written as [18]

$$\lambda_1 = \frac{\mu_1 \mu_2}{\beta_1} \frac{k_{z_2}^2 + \beta_1^2}{(\mu_2^2 \beta_1^2 + \mu_1^2 k_{z_2}^2)}, \tag{2.25}$$

$$\lambda_3 = \frac{\mu_3 \mu_2}{\beta_3} \frac{k_{z_2}^2 + \beta_3^2}{(\mu_2^2 \beta_3^2 + \mu_3^2 k_{z_2}^2)}, \tag{2.26}$$

where λ_1 and λ_3 are the penetration of guided wave from the guiding layer into the substrate and cladding layers, respectively.

When a light beam undergoes a total internal reflection at the interface of two different media, the reflected light beam experiences a lateral shift in the plane of incidence from the position predicted by the geometrical optics because each plane wave component undergoes a different phase change [28]. This shift is known as Goos-Hänchen (GH) shift. GH-shifts at the film-substrate (GH_1) and the film-cladding (GH_3) interfaces are given by [66,67]

$$GH_1 = \frac{\lambda}{\pi} \frac{\tan \gamma}{\sqrt{N^2 - n_1^2}}, \tag{2.27}$$

$$GH_3 = \frac{\lambda}{\pi} \frac{\tan \gamma}{\sqrt{N^2 - n_3^2}}, \tag{2.28}$$

with $\gamma = \sin^{-1}\left(\dfrac{N}{n_2}\right)$ is the incidence angle.

2.6. Numerical results

In the analysis below we have assumed the wavelength of ND Yag laser ($\lambda = 1064$ nm), the substrate to be SiO_2 with $n_1 = 1.5341$ ($\varepsilon_1 = 2.35$), the cladding to be water of $n_3 = 1.33$ ($\varepsilon_3 = 1.77$), the core layer to be LHM which is

characterized by ε_2 and μ_2 given by Eqs.(2.1,2.2) with $\omega_p = 2\omega$, $\omega_0 = 0.4\omega_p$ and $\mu_1 = \mu_3 = 1$. Eq.(2.3) has been solved numerically for the effective refractive index. The sensitivity, the power flow, the penetration depth, and the Goos-Hanchen shift are calculated using the above set of equations. Figures 2.2 and 2.3 show the variation of the real and imaginary parts of the sensitivity of the proposed sensor with the thickness of the LHM guiding layer and the electron scattering rate γ. As can be seen from the figures, the sensitivity is negative and has a peak at a specific value of the guiding layer thickness (d). The absolute value of the sensitivity decays towards lower values for high values of d due to the high field confinement. The absolute values of the real and imaginary parts of the sensitivity increase as γ decreases.

Fig. 2.2. The real part of the sensitivity of the proposed sensor versus the thickness of the guiding layer for different values of the electron scattering rate for $\lambda = 1064$ nm, $\varepsilon_1 = 2.35$, $\varepsilon_3 = 1.77$, $\mu_1 = 1$, $\mu_3 = 1$ and $F = 0.56$.

Fig. 2.3. The imaginary part of the sensitivity of the proposed sensor versus the thickness of the guiding layer for different values of the electron scattering rate for $\lambda = 1064$ nm, $\varepsilon_1 = 2.35$, $\varepsilon_3 = 1.77$, $\mu_1 = 1$, $\mu_3 = 1$ and $F = 0.56$.

It is very important to compare the sensitivity obtained for the proposed senor and that of the conventional three-layer slab waveguide sensor with positive index guiding layer. Figure 2.4 shows the absolute value of the real part of the sensitivity of the proposed sensor with the negative index material guiding layer and the sensitivity (S_l) of the conventional three-layer slab waveguide sensor with positive index material guiding layer. It is clear from the figure that the proposed sensor has an improved sensitivity. The improvement may be attributed to the property of amplification of evanescent waves observed in LHMs [65].
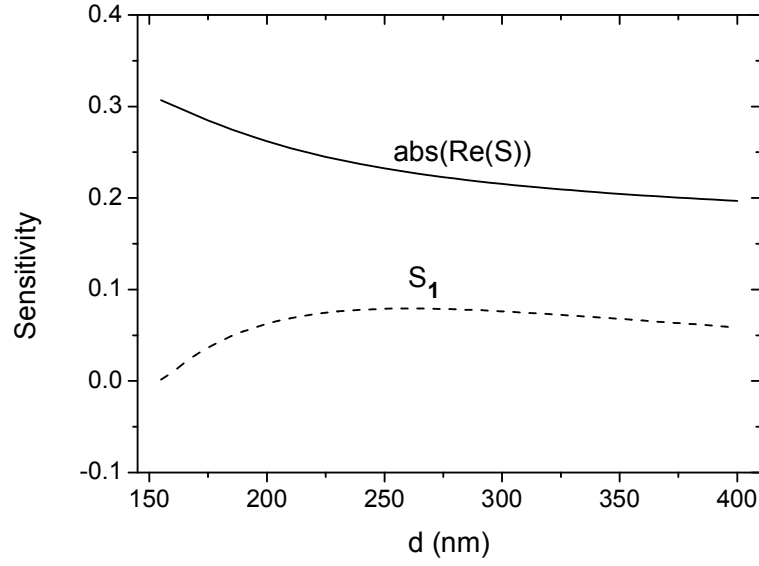
Fig. 2.4. Comparison between the sensitivity of the proposed sensor and that of the conventional sensor (S_1) for $\lambda = 1064$ nm, $\varepsilon_1 = 2.35$, $\varepsilon_3 = 1.77$, $\mu_1 = 1$, $\mu_3 = 1$, $\gamma = 0.012\omega_p$, and $F = 0.56$. $S_1 =$ sensitivity of conventional structure.

The negative value of the sensitivity of the proposed structure is considered as a new feature that has not been observed in slab waveguide optical sensors. To clarify this point, we plot the real part of the effective refractive index as a function of d for different values of the cladding index. In the case of the proposed sensor, the effective refractive index N decreases as the cladding index n_3 increases as shown in Fig. 2.5. This explains the negative value of the sensitivity which is the differentiation of N with respect to n_3. On the other hand, N increases as n_3 increases for the conventional sensor.
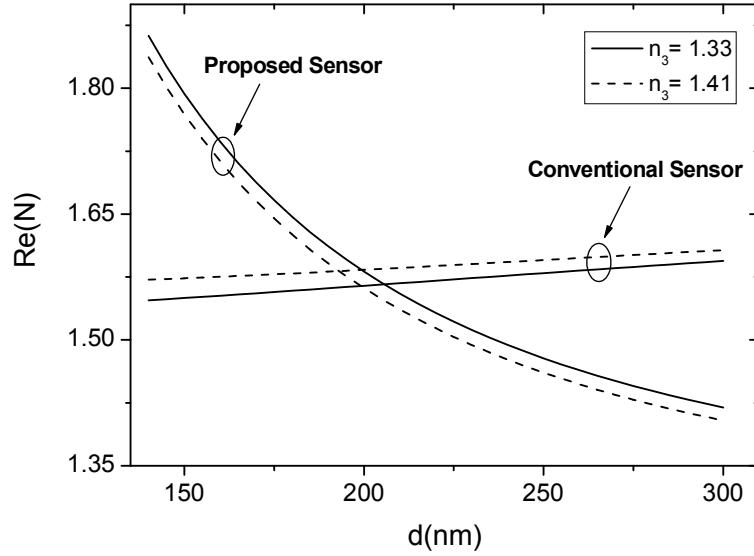
Fig. 2.5. The real part of the effective refractive index of the proposed sensor and that of the conventional sensor versus the thickness of the guiding layer for different values of the index of the cladding for $\lambda = 1064$ nm, $\varepsilon_l = 2.35$, $\mu_l = 1$, $\mu_3 = 1$, $\gamma = 0.012\omega_p$ and $F = 0.56$.

In Figs. 2.6 and 2.7, the real and imaginary parts of the sensitivity are plotted respectively versus the thickness of the guiding layer for different values of the fractional area of the unit cell occupied by the split ring. As can be seen from the figures, Re(S) and Im(S) exhibit different behaviors with F. In contrary to Im(S), the absolute value of Re(S) increases with increasing F for a given value of d.

Figures 2.8, 2.9, and 2.10 show the real part of the power transported in the substrate, the guiding film, and the cladding, respectively. Many interesting features can be observed in these figures. First, the powers transported in the substrate and the cladding show the same behavior with γ. Decreasing γ enhances both of the powers. The enhancement of Re(P_3) with decreasing γ explains the enhancement of the Re(S) with decreasing γ observed in Fig. 2.2. The sensitivity of evanescent field sensors is totally dependent on the power transported in the analyte medium (the material to be detected in the cladding

layer). Second, the negative value of the film power is the most important feature that can be seen in Fig. 2.9. This is one of the main differences between LHM and conventional materials. In LHM, the Poynting's vector $\boldsymbol{S}$ always forms a left-handed set with the vectors $\boldsymbol{E}$ and $\boldsymbol{H}$. Accordingly, $\boldsymbol{S}$ and the propagation vector $\boldsymbol{k}$ are in opposite directions. Thus, it is clear that LHMs are substances with a so-called negative group velocity, which occurs in particular in anisotropic substances or when there is spatial dispersion. In brief, Fig. 2.9 emphasizes the fact that in LHMs the phase velocity is opposite to the energy flow. Third, the effect of γ on the power transported in the film is barely detectable in the range considered for γ due to the large value of $Re(P_2)$ compared to $Re(P_1)$ and $Re(P_3)$.
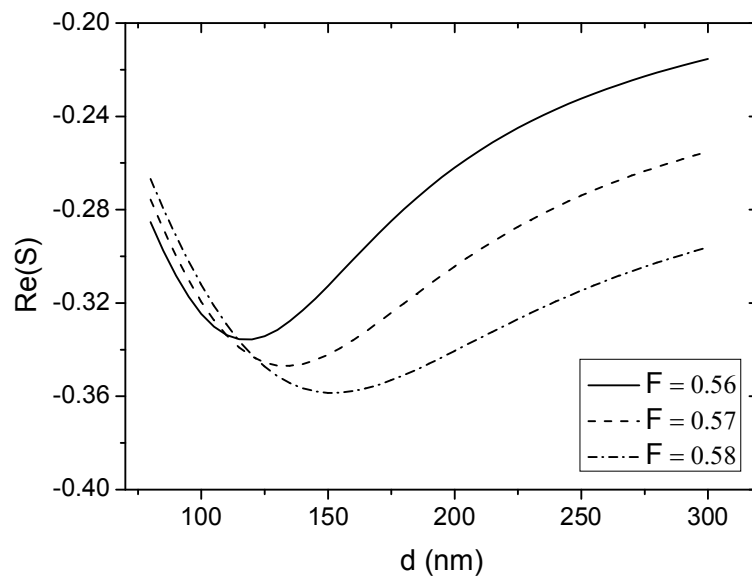
Fig. 2.6. The real part of the sensitivity of the proposed sensor versus the thickness of the guiding layer for different values of the fractional area of the unit cell occupied by the split ring for $\lambda=1064$ nm, $\varepsilon_1 = 2.35$, $\varepsilon_3 = 1.77$, $\mu_1 = 1$, $\mu_3=1$ and $\gamma = 0.012\omega_p$.
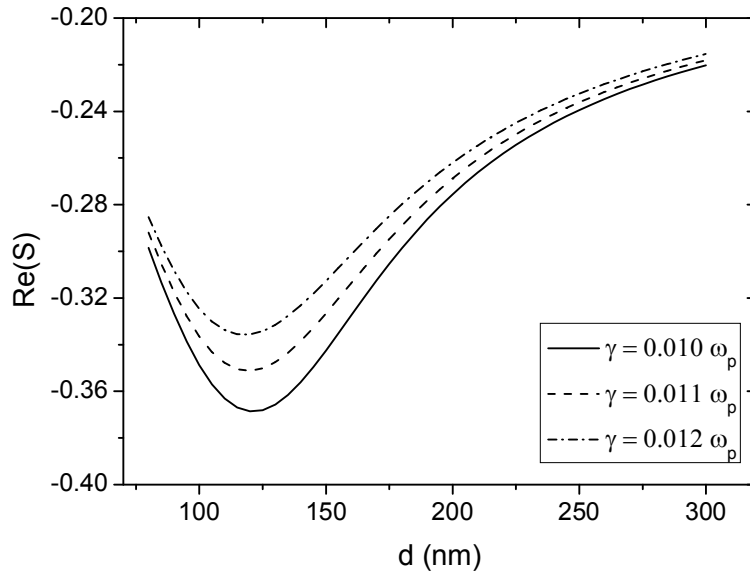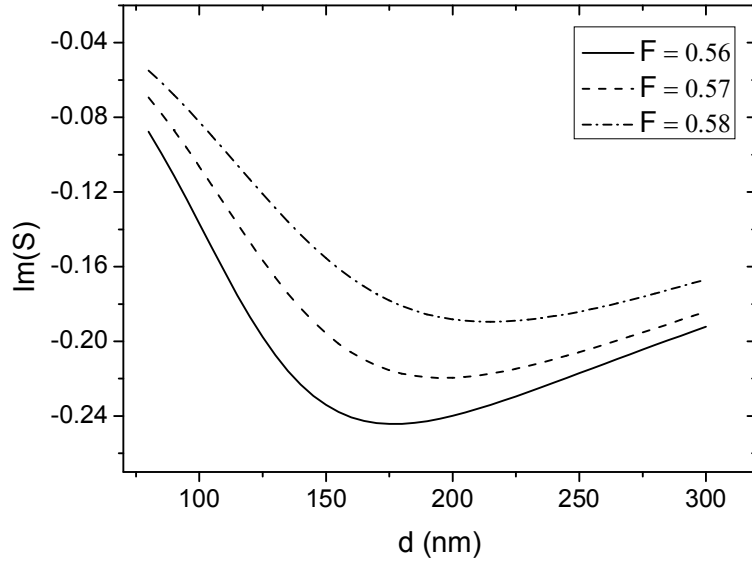
Fig. 2.7. The imaginary part of the sensitivity of the proposed sensor versus the thickness of the guiding layer for different values of the fractional area of the unit cell occupied by the split ring for $\lambda = 1064$ nm, $\varepsilon_1 = 2.35$, $\varepsilon_3 = 1.77$, $\mu_1 = 1$, $\mu_3 = 1$ and $\gamma = 0.012\omega_p$.

Fig. 2.8. The real part of the power flowing within the substrate layer versus the thickness of the guiding layer for different values of the electron scattering rate for $\lambda = 1064$ nm, $\varepsilon_1 = 2.35$, $\varepsilon_3 = 1.77$, $\mu_1 = 1$, $\mu_3 = 1$, and $F = 0.56$.
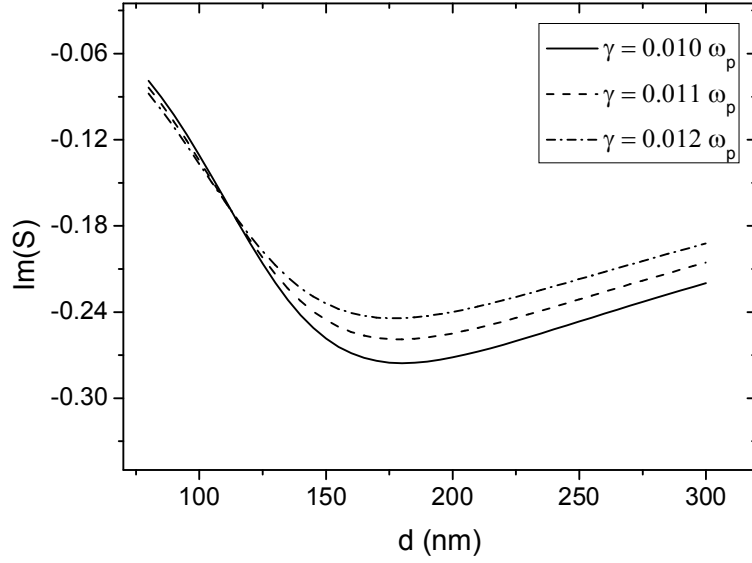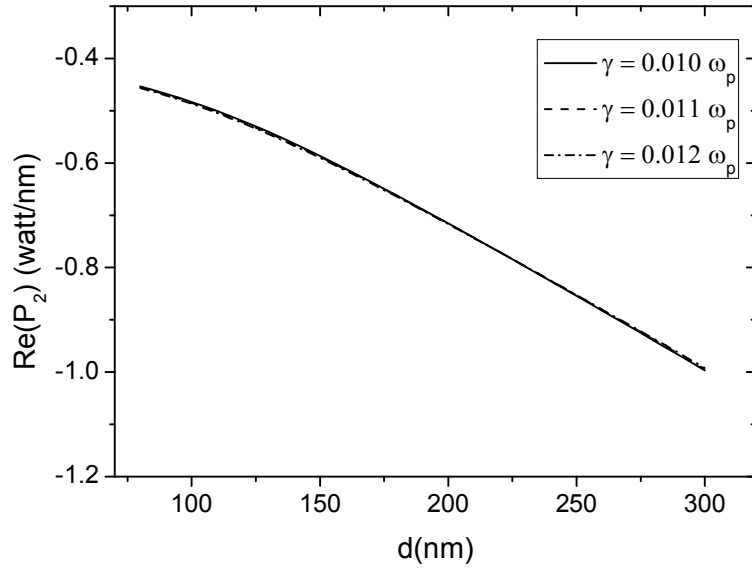
Fig. 2.9. The real part of the power flowing through the guiding layer versus the thickness of the guiding layer for different values of the electron scattering rate for $\lambda = 1064$ nm, $\varepsilon_1 = 2.35$, $\varepsilon_3 = 1.77$, $\mu_1 = 1$, $\mu_3 = 1$, and F=.56.
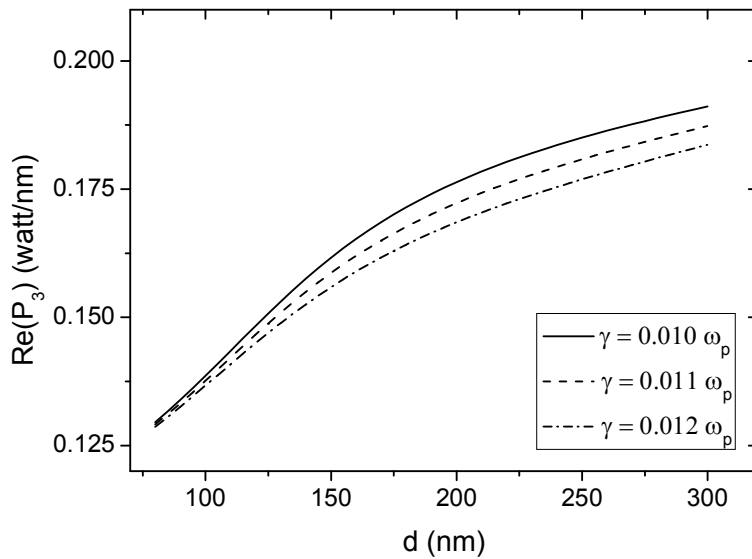
Fig. 2.10. The real part of the power flowing through the cladding layer versus the thickness of the guiding layer for different values of the electron scattering rate for $\lambda = 1064$ nm, $\varepsilon_1 = 2.35$, $\varepsilon_3 = 1.77$, $\mu_1 = 1$, $\mu_3 = 1$, and F=0.56.

Figures 2.11, 2.12, and 2.13 show the imaginary parts of the power transported within the three layers. The powers transported in the substrate, film, and cladding show the same behavior with γ. A little enhancement could be achieved by decreasing γ.
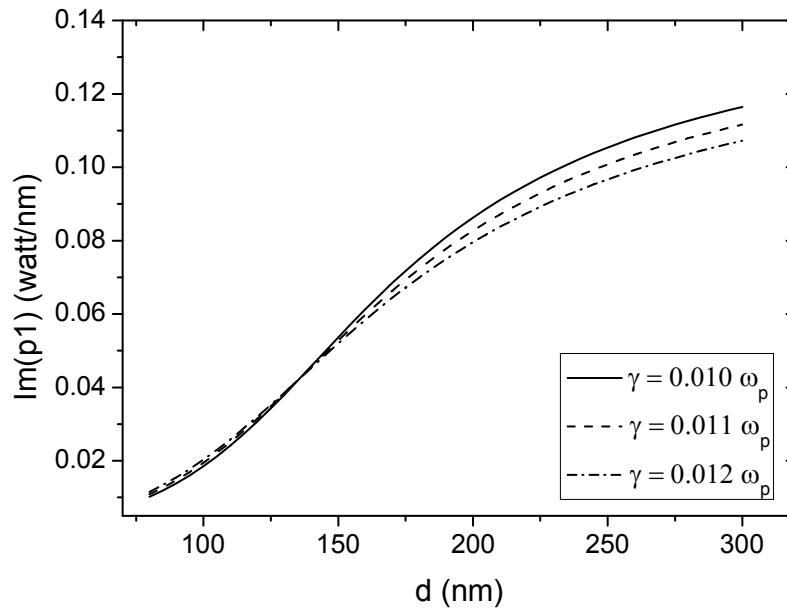
Fig. 2.11. The imaginary part of the power flowing through the substrate layer versus the thickness of the guiding layer for different values of the electron scattering rate for $\lambda = 1064$ nm, $\varepsilon_1 = 2.35$, $\varepsilon_3 = 1.77$, $\mu_1 = 1$, $\mu_3 = 1$, and F= 0.56.
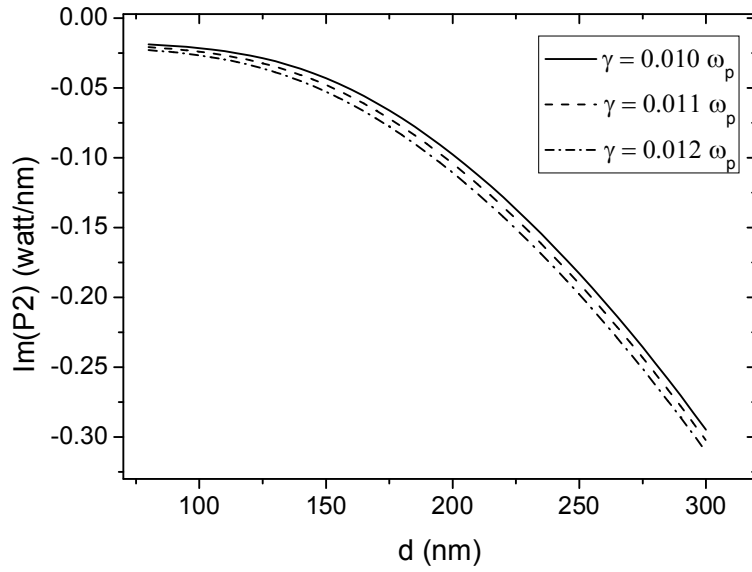
Fig. 2.12. The imaginary part of the power flowing through the guiding layer versus the thickness of the guiding layer for different values of the electron scattering rate for $\lambda = 1064$ nm, $\varepsilon_1 = 2.35$, $\varepsilon_3 = 1.77$, $\mu_1 = 1$, $\mu_3 = 1$, and F=0.56.
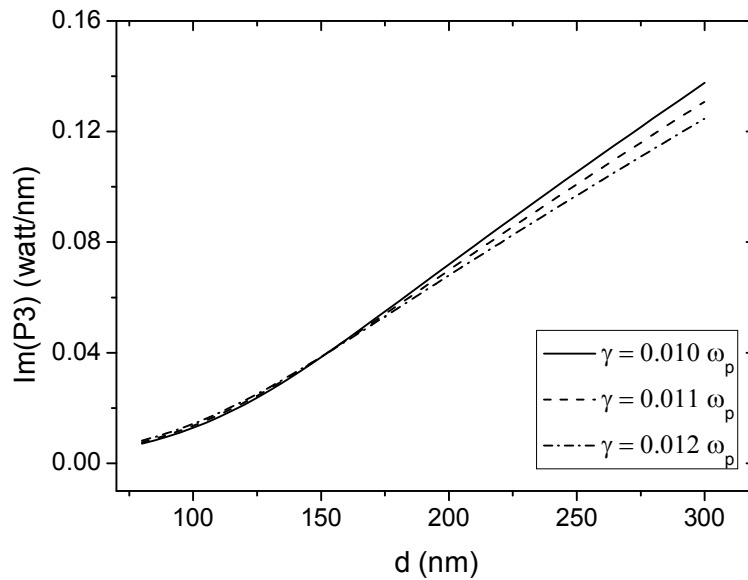
Fig. 2.13. The imaginary part of the power flowing through the cladding layer versus the thickness of the guiding layer for different values of the electron scattering rate for $\lambda = 1064$ nm, $\varepsilon_1 = 2.35$, $\varepsilon_3 = 1.77$, $\mu_1 = 1$, $\mu_3 = 1$, and F=0.56.

In Fig. 2.14 the real part of confinement factors are plotted versus the thickness of the guiding layer for different values of the electron scattering rate γ. Figure 2.15 shows the real part of confinement factors versus the thickness of the guiding layer for different values of the fractional area of the unit cell occupied by the split ring (F). For sensing purposes, it is significant to study the effect of the LHM core layer parameters on the cladding confinement factor. As can be seen from the figures, the effect of γ on Γ_c is barely seen whereas the effect of F is relatively considerable. The higher the value of F, the more the fractional power in the cladding especially for d = 100 nm. This is in agreement with the observations seen from Fig. 2.6.
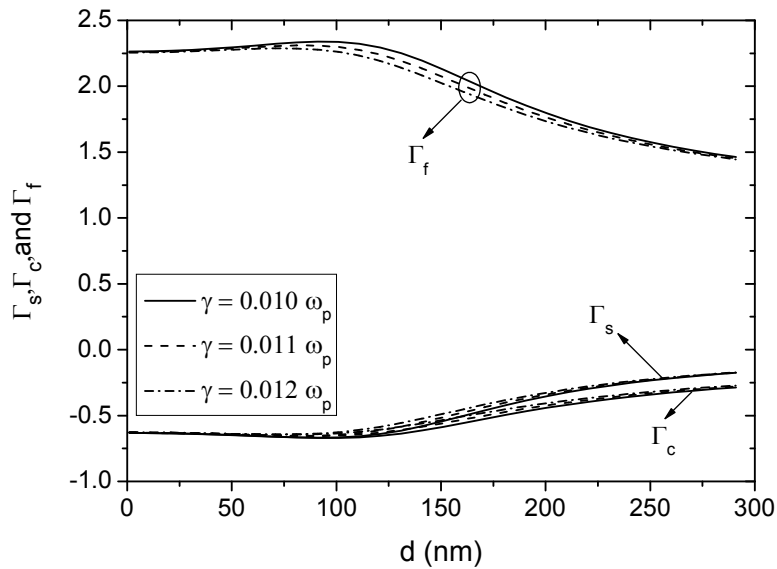
Fig. 2.14. The real part of confinement factors as a function of d and γ for λ = 1064 nm, ε_1 = 2.35, ε_3 = 1.77, μ_1 = 1, μ_3 =1, and F = 0.56.
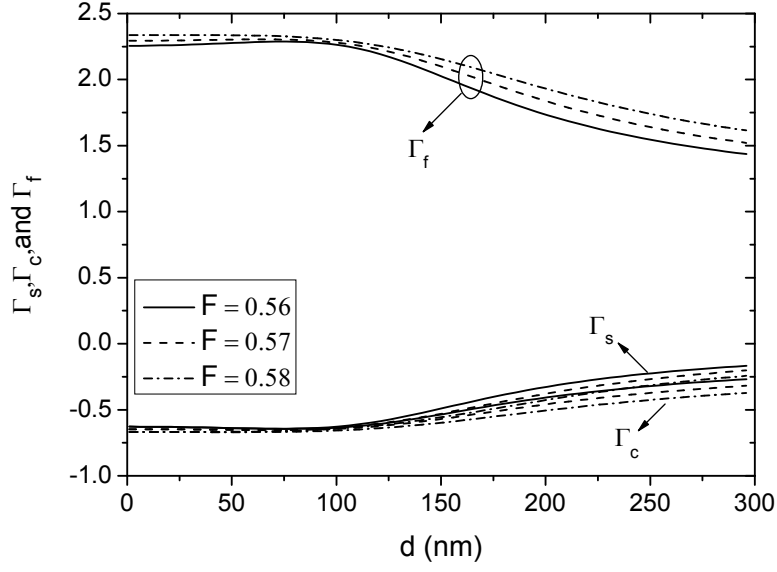
Fig. 2.15. The real part of confinement factors as a function of d and F for $\lambda = 1064$ nm, $\varepsilon_1 = 2.35$, $\varepsilon_3 = 1.77$, $\mu_1 = 1$, $\mu_3 = 1$, and $\gamma = 0.012\ \omega_p$.

In order to study all parameters of the proposed structure, we plot the penetration depth and the GH shifts as a function of the guiding layer thickness for different values of the electron scattering rate γ as shown in Figs. 2.16 and 2.17, respectively. Both of them can be treated as a probe for detection the changes in the refractive index of an aqueous cladding. In the analysis above, we have adopted the effective refractive index as a probe for detection the cladding index changes which is one of the most commonly used techniques in slap waveguide sensors. Generally, any cladding-index dependent waveguide parameter can be used as the probe for optical sensing purposes provided that this parameter is practically measurable. Both the penetration depth and the GH shift are dependent on the cladding index and measurable. For example, several techniques have been developed for measuring the GH shift. Bretenaker et al. experimentally investigated the measurement of the GH shift for only one reflection [66]. His method uses the high sensitivity of the eigenstates of a quasi-isotropic laser to small perturbations to measure GH shift for angles of incidence both below and above the critical angle. Another approach was

proposed to measure the GH shift [67] based on the modulation of the polarization state of a laser by an electro-optic modulator combined with a precise measurement of the resulting spatial displacement with a position-sensitive detector. The sensitivity of any waveguide parameter to changes in the cladding index is given as the differentiation of that parameter with respect to n_3.
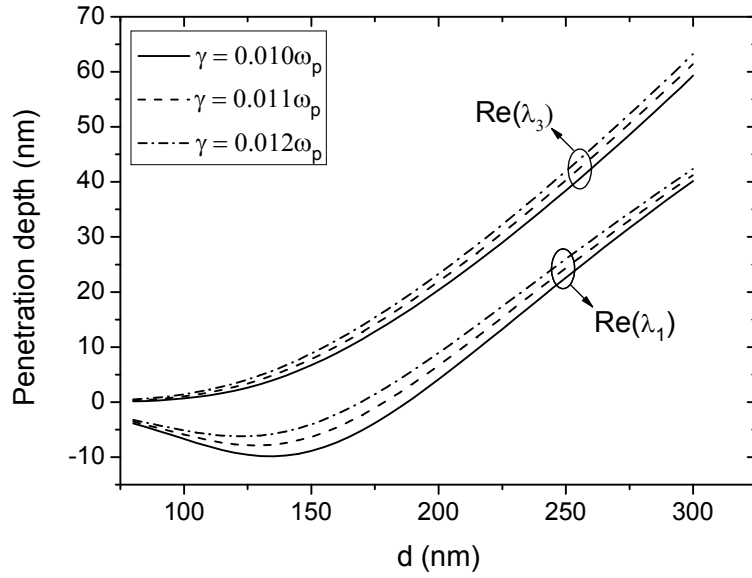
Fig. 2.16. The penetration depth in the substrate and the cladding layers versus the thickness of the guiding layer for different values of the electron scattering rate for $\lambda = 1064$ nm, $\varepsilon_1 = 2.35$, $\varepsilon_3 = 1.77$, $\mu_1 = 1$, $\mu_3 = 1$ and $F = 0.56$.
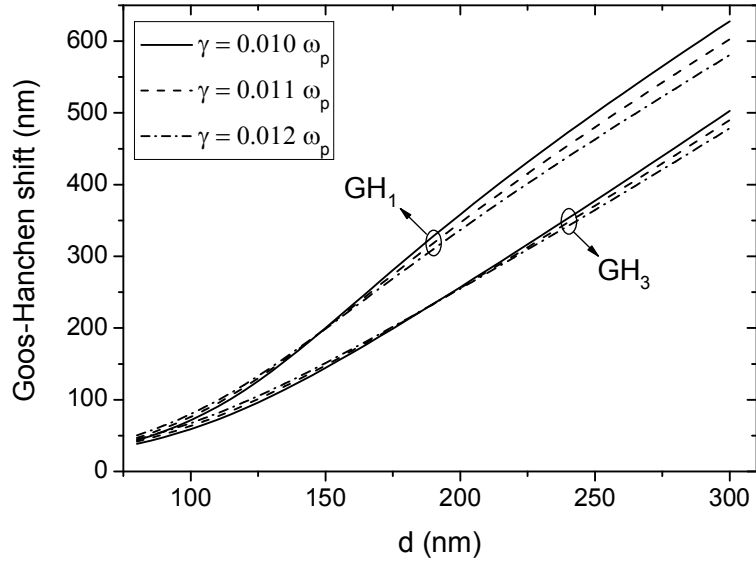
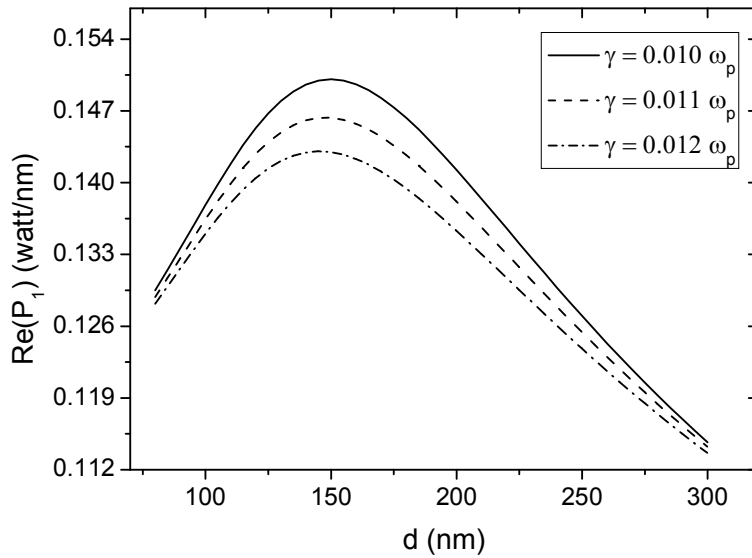Fig. 2.17. The Goos-Hanchen shift in the substrate and the cladding layers versus the thickness of the guiding layer for different values of the electron scattering rate for $\lambda = 1064$ nm, $\varepsilon_1 = 2.35$, $\varepsilon_3 = 1.77$, $\mu_1 = 1$, $\mu_3 = 1$ and $F = 0.56$.

Chapter three

Slab waveguide optical sensor with left handed material as a core layer: TM-mode

In this chapter, a symmetric three-layer slab waveguide with a left handed material serves as a guiding layer is examined analytically for cover refractive index detection. The dispersion relation of TM mode for the proposed waveguide will be investigated. The sensitivity of the proposed sensor to changes in the cover refractive index and the power flowing within each layer will be presented.

3.1. Structure analysis

Figure 3.1 shows a schematic of the proposed sensor configuration. We consider a slab waveguide with LHM thin film of thickness d occupying the region $0 < z < d$, which is characterized by an electric permittivity ε_2 and magnetic permeability μ_2, given by Eqs.(2.1,2.2). The slab is sandwiched between two semi-infinite media occupying the regions $z < 0$ and $z > d$ and having parameters (ε_1, μ_1) and (ε_3, μ_3), respectively. To create a LHM medium, an array of wires interspersed with an array of split ring resonators has been used in the literature [68]. The thin wire array has been shown to yield effective electric permittivity and magnetic permeability given by Eqs. (2.1) and (2.2).
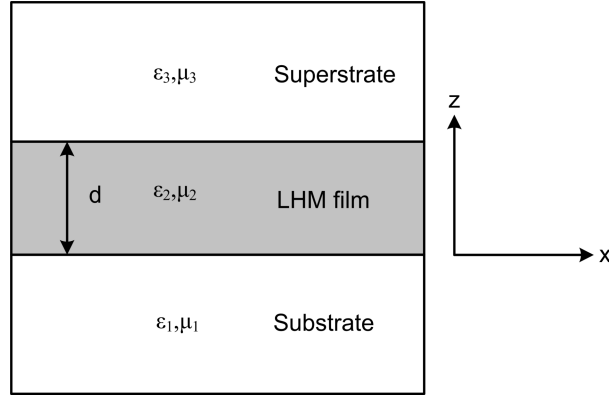
Fig. 3.1. Schematic structure of the proposed sensor.

3.2 The dispersion relation

Solving Maxwell's equations for the three-layer structure yields the solutions for the time harmonic magnetic field given by

$$H_y = \begin{cases} Ae^{\beta_1 z}e^{ik_x x} & \text{Substrate region} \\ (Be^{-\beta_2 z} + Ce^{\beta_2 z})e^{ik_x x} & \text{Film region} \\ De^{-\beta_3(z-d)}e^{ik_x x} & \text{Superstrate region} \end{cases} \quad (3.1)$$

Equations (1.120) and (1.121) for TM modes have been employed to calculate E_x and E_z

$$E_x = \begin{cases} -i\dfrac{\beta_1 A}{\omega\varepsilon_o\varepsilon_1}e^{\beta_1 z}e^{ik_x x} & \text{Substrate region} \\ i\dfrac{\beta_2}{\omega\varepsilon_o\varepsilon_2}\left(-Be^{-\beta_2 z} + Ce^{\beta_2 z}\right)e^{ik_x x} & \text{Film region} \\ -i\dfrac{\beta_3 D}{\omega\varepsilon_o\varepsilon_3}e^{-\beta_3(z-d)}e^{ik_x x} & \text{Superstrate region} \end{cases} \quad (3.2)$$

57

$$
E_z = \begin{cases} \dfrac{k_x A}{\omega \varepsilon_o \varepsilon_1} e^{\beta_1 z} e^{ik_x x} & \text{Substrate region} \\[3mm] \dfrac{k_x}{\omega \varepsilon_o \varepsilon_2} \left(B e^{-\beta_2 z} + C e^{\beta_2 z} \right) e^{ik_x x} & \text{Film region} \\[3mm] \dfrac{k_x D}{\omega \varepsilon_o \varepsilon_3} e^{-\beta_3 (z-d)} e^{ik_x x} & \text{Superstrate region} \end{cases} \tag{3.3}
$$

where $\beta_j = -ik_{z,j} = (k_x^2 - \varepsilon_j \mu_j k_0^2)^{1/2}$, j = 1, 2, and 3, $k_x = k_0 N$, $k_0 = \dfrac{2\pi}{\lambda}$, λ is the vacuum wavelength of the guided light, and N is the effective refractive index.

The constants A, B, C, D, and the longitudinal propagation constants k_x can be determined by applying the boundary conditions which require that the **E** and **H** components parallel to the interfaces are continuous. Thus, the amplitudes are related to each through the relations

$$
B = \frac{A}{2}\left(1 - i \frac{\varepsilon_2}{\varepsilon_1} \frac{\beta_1}{k_{z,2}} \right), \tag{3.4}
$$

$$
C = \frac{A}{2}\left(1 + i \frac{\varepsilon_2}{\varepsilon_1} \frac{\beta_1}{k_{z,2}} \right), \tag{3.5}
$$

$$
D = A\left(1 - i \frac{\varepsilon_2}{\varepsilon_1} \frac{\beta_1}{k_{z,2}} \right)\left(\frac{\varepsilon_3 k_{z,2}}{\varepsilon_3 k_{z_2} + i\beta_3 \varepsilon_2} \right) e^{ik_{z,2} d}. \tag{3.6}
$$

Applying the continuity requirements at z = 0 and z = d and after some manipulation, we obtain the dispersion relation for bulk polariton of TM mode as

$$
\left(\frac{k_{z,2}}{\varepsilon_2} \right)^2 - \cot(k_{z,2} d)\left(\frac{\beta_1}{\varepsilon_1} + \frac{\beta_3}{\varepsilon_3} \right)\left(\frac{k_{z,2}}{\varepsilon_2} \right) - \left(\frac{\beta_1}{\varepsilon_1} \frac{\beta_3}{\varepsilon_3} \right) \mp m\pi = 0. \tag{3.7}
$$

3.3 The sensitivity

Differentiating Eq.(3.7) with respect to N, the sensitivity of the proposed sensor for TM mode is found to be given by

$$S = \frac{G_1}{a_c} \frac{n_3}{NX_c} \left(1 + 2\frac{a_n X_c^2}{n_3^2}\right) \left(k_0 d + G_1 \frac{q_c}{a_c} + G_2 \frac{q_s}{a_s}\right)^{-1},$$ (3.8)

where

$$a_s = \frac{\varepsilon_1}{\varepsilon_2}, \ a_c = \frac{\varepsilon_3}{\varepsilon_2}, \ a_n = \frac{1}{n_2^2 - N^2}, \ X_s = \frac{\beta_1}{k_{z,2}}, \ X_c = \frac{\beta_3}{k_{z,2}},$$

$$G_1 = \frac{1}{1 + \left(\dfrac{X_c}{a_c}\right)^2}, \ G_2 = \frac{1}{1 + \left(\dfrac{X_s}{a_s}\right)^2}, \ q_s = \frac{1 + X_s^2}{X_s}, \text{ and } q_c = \frac{1 + X_c^2}{X_c}.$$

3.4 The power propagating

To study the power propagating in the structure, the time-averaged Poynting vector $S_x = \mathrm{Re}[(\vec{E} \times \vec{H}) \cdot \hat{a}_x]$ is calculated. The total energy flux can be calculated as $\int_{-\infty}^{\infty} S_x \, dz$, from which we obtain,

$$P_1 = \frac{k_x |A|^2}{4\omega\varepsilon_o n_1^2 \beta_1},$$ (3.9)

$$P_2 = \frac{k_x \mu_2}{2\omega\varepsilon_o n_2^2} \left\{ -i\frac{|B|^2}{2k_{z,2}}(e^{2ik_{z,2}d} - 1) + i\frac{|C|^2}{2k_{z,2}}(e^{-2ik_{z,2}d} - 1) + 2BCd \right\},$$ (3.10)

$$P_3 = \frac{k_x |D|^2}{4\omega\varepsilon_o n_3^2 \beta_3},$$ (3.11)

where the amplitudes A, B, C, and D are related to each through the Eqs.(3.4-3.6). The confinement factor for the substrate, film, cladding layers are respectively given by

$$\Gamma_s = \frac{1}{\varepsilon_1 \beta_1} \left[\frac{1}{\varepsilon_1 \beta_1} + \frac{i}{4\varepsilon_2 k_{z,2}} \left(c_-^2 a_+ - c_+^2 a_- - 4ik_{z,2} dc_- c_+ \right) - \frac{\varepsilon_3 k_{z,2}^2 c_-^2}{\beta_3 (\varepsilon_2 \beta_3 - i\varepsilon_3 k_{z,2})^2} e^{2ik_{z,2}d} \right]^{-1}$$

(3.12)

$$\Gamma_f = \frac{\dfrac{i}{8\mu_2 k_{z,2}} \left(c_-^2 a_+ - c_+^2 a_- - 4ik_{z,2} dc_- c_+ \right)}{\left[\dfrac{1}{2\varepsilon_1 \beta_1} + \dfrac{i}{8\varepsilon_2 k_{z,2}} \left(c_-^2 a_+ - c_+^2 a_- - 4ik_{z,2} dc_- c_+ \right) - \dfrac{\varepsilon_3 k_{z,2}^2 c_-^2}{2\beta_3 (\varepsilon_2 \beta_3 - i\varepsilon_3 k_{z,2})^2} e^{2ik_{z,2}d} \right]}$$

(3.13)

$$\Gamma_c = \frac{-4 \dfrac{\mu_3 k_{z,2}^2 c_-^2}{\beta_3 (\mu_2 \beta_3 - i\mu_3 k_{z,2})^2} e^{2ik_{z,2}d}}{\left[\dfrac{1}{\varepsilon_1 \beta_1} + \dfrac{i}{4\varepsilon_2 k_{z,2}} \left(c_-^2 a_+ - c_+^2 a_- - 4ik_{z,2} dc_- c_+ \right) - \dfrac{\varepsilon_3 k_{z,2}^2 c_-^2}{\beta_3 (\varepsilon_2 \beta_3 - i\varepsilon_3 k_{z,2})^2} e^{2ik_{z,2}d} \right]}$$

(3.14)

where

$$c_\pm = \left(1 \pm i \frac{\varepsilon_2}{\varepsilon_1} \frac{\beta_1}{k_{z,2}} \right), \tag{3.15}$$

$$a_\pm = 1 - e^{\pm 2ik_{z,2}d}. \tag{3.16}$$

3.5. Numerical results

In our analysis we have considered symmetric slab waveguide with water surrounding medium with $n_1 = n_3 = 1.33$ ($\varepsilon_1 = \varepsilon_3 = 1.77$) and $\mu_1 = \mu_3 = 1$ at the wavelength of ND Yag laser ($\lambda = 1064$ nm).

The real and imaginary parts of the sensitivity of the proposed sensor as a function of thickness of the LHM film and for different values of γ are plotted in Figs. 3.2 and 3.3, respectively. The two figures show a negative sensitivity which means that the dependence of the effective refractive index on the cladding index has a negative gradient. The real part of the effective refractive index is much more sensitive to variations of the cladding index than the imaginary part. For instance, at a guiding layer thickness 150 nm and $\gamma =$

$0.010\omega_p$, the calculated values of Re(S) = -1.4833 whereas Im(S) = -0.0554, which means that Re(S) is 26.77 times the Im(S). This is simply because the cladding index is real and therefore any change in it has a greater impact on the real part of the effective refractive index. As seen in Fig. 3.3, the sensitivity of the imaginary part of the effective index can be slightly improved with increasing γ, whereas the Re(S), due to its high value, is barely affected with changing γ in the considered range of γ. In general, both the real and imaginary parts of S show the same behavior with the thickness of the guiding LHM layer. The absolute value of both parts of the sensitivity maximizes for low values of d and decays with increasing the thickness. In principle, the sensing operation is performed by the evanescent optical field extending from the thin guiding film into the cladding medium. This part of the guided field is generally few percent and decays with increasing the thickness d due to the high confinement of the guided mode. The behavior of both parts of the sensitivity with d is similar to that obtained for the sensitivity of the conventional three layer waveguide with a positive index material guiding layer with a reverse symmetry configuration [28,29].

It is clear that the proposed sensor has an improved sensitivity compared to the conventional ones given in the literature in different forms. To illustrate this point, we assume a symmetric three layer waveguide with a lossless positive index material guiding layer. The sensitivity of such a structure is given in Refs. 21 and 24. In Fig 3.4, the absolute value of the real part of the sensitivity of the proposed sensor and the sensitivity of the conventional structure are plotted as a function of thickness d. As seen from the figure, the sensitivity of the proposed sensor is much higher than that of the conventional three layer waveguide sensor. The sensitivity improvement compared with the conventional three layer waveguide sensor is critically dependent on the thickness of the guiding layer, e.g., for d = 80 nm, d = 100 nm, and d = 150 nm the enhancement is approximately a factor of 5.82, 5.49, and 3.27, respectively.
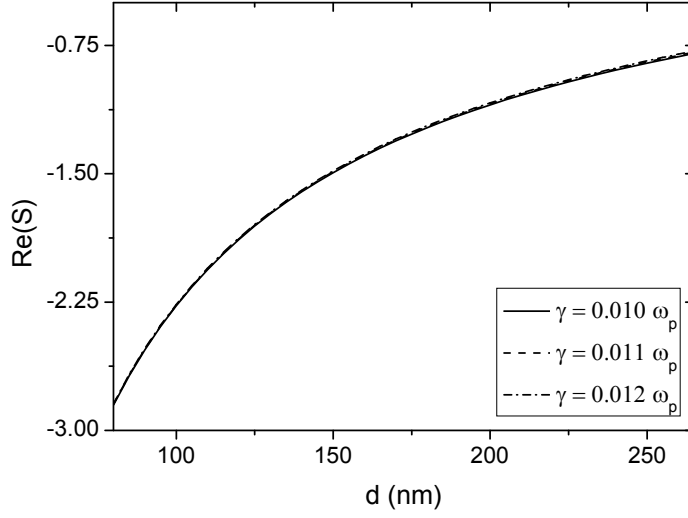
Fig. 3.2. The real part of the sensitivity of the proposed sensor versus the thickness of the guiding LHM layer for different values of the electron scattering rate for $\lambda = 1064$ nm, $\varepsilon_1 = \varepsilon_3 = 1.77$, $\mu_1 = \mu_3 = 1$, $F = 0.58$, $\omega_0 = 0.4\omega_p$, and $\omega_p = 2\omega$.
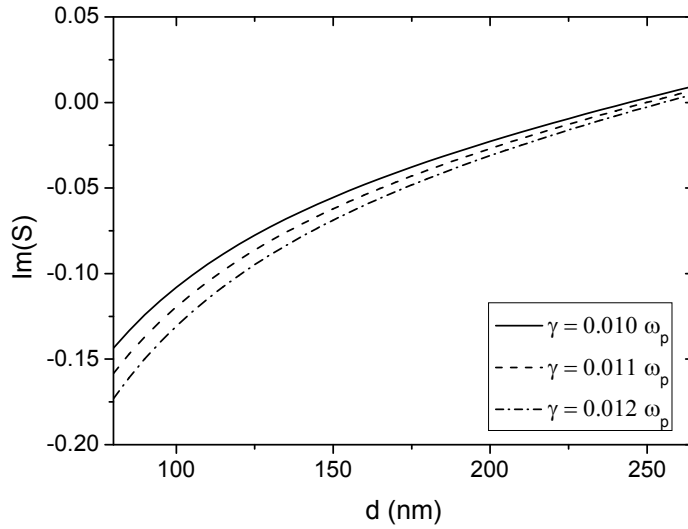
Fig. 3.3. The imaginary part of the sensitivity of the proposed sensor versus the thickness of the guiding LHM layer for different values of the electron scattering rate for $\lambda = 1064$ nm, $\varepsilon_1 = \varepsilon_3 = 1.77$, $\mu_1 = \mu_3 = 1$, $F = 0.58$, $\omega_0 = 0.4\omega_p$, and $\omega_p = 2\omega$.
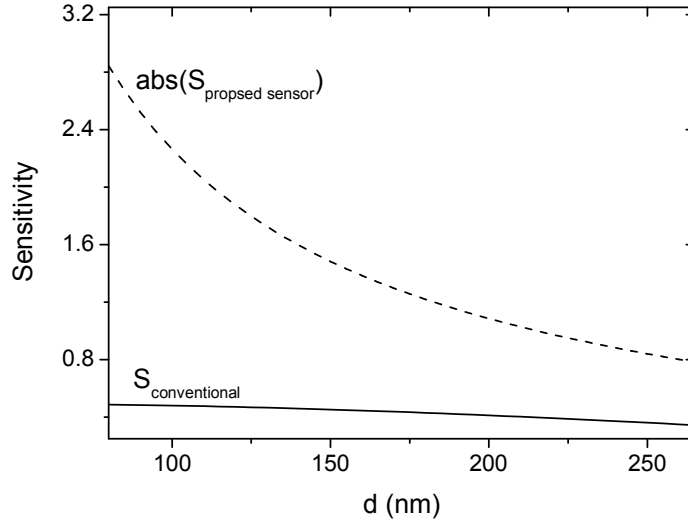
Fig. 3.4. The absolute value of the real part of the sensitivity of the proposed sensor and the sensitivity of the conventional sensor as a functions of d for $\lambda = 1064$ nm, $\varepsilon_1 = \varepsilon_3 = 1.77$, $\mu_1 = \mu_3 = 1$, $\gamma = 0.012\omega_p$, $F = 0.58$, $\omega_0 = 0.4\omega_p$, and $\omega_p = 2\omega$.

This sensitivity enhancement is attributed to the amplification of evanescent waves caused by LHMs. It was verified that LHMs with low loss can focus light onto an area smaller than a square wavelength in near fields [69]. This super-resolution is also attributed the important feature of LHMs which is amplification of evanescent waves [70].

In order to optimize the proposed structure, it is significant to study the sensitivity dependence on the different parameters of the LHM guiding layer. We here restrict ourselves to the real part of the sensitivity. As seen by Eqs. (2.1,2.2), ε_2 and μ_2 are critically dependent on ω, ω_p, and ω_o. Figure 3.5 shows the real part of the sensitivity as a function of ω_p/ω for different guiding layer thicknesses. In the figure, the range $1.68 < \omega_p/\omega < 2$ (in GHz) has been considered in which the real parts of ε_2 and μ_2 are both negative to make sure that the guiding layer is made of a left-handed material. A number of interesting features can be observed in the figure. There is an optimum value of

ω_p/ω at which the Re(S) peaks and this optimum value is dependent on the thickness of the guiding layer. The optimum value of ω_p/ω shifts towards higher values as the thickness of the guiding layer increases. For $d = 100$ nm, the optimum value of ω_p/ω is 1.688 whereas it is 1.698 for $d = 145$ nm. The value of the sensitivity at the peak is critically dependent on the thickness of the guiding LHM layer. In the considered range of ω_p/ω and d, the sensitivity at the peaks ranges between -8 to -16. The most important feature is that through proper choice of ω_p/ω and d, the Re(S) may reach a value of order -16 which means the enhancement factor of the sensitivity of the proposed sensor could be of order 32.

Figure 3.6 shows the real part of the sensitivity as a function of the thickness of the LHM guiding layer for different values of the resonance frequency ω_o. A considerable increase in the absolute value of the Re(S) is observed with decreasing ω_o. The impact of ω_o on the Re(S) is much greater than that of γ. It is well-known that LHMs are artificial multifunctional materials that gain its material properties from its structure rather than inheriting them directly from the materials it is composed of. Thus the LHM parameters (ω_p, ω_o, γ) can be controlled by adjustment of the structure size. For example, in a recent study, the resonance frequency band of a rectangular periodic band is found to be shifted and broadened from low frequency to high frequency by adjustment of the corresponding structure size [71]. Therefore, the LHM parameters (ω_p, ω_o, γ) can be adjusted to attain a considerable sensitivity enhancement.

Figure 3.7 shows the imaginary part of the sensitivity as a function of the thickness of the guided layer for different values of the resonance frequency ω_o, the absolute value of the imaginary part of the sensitivity decreases as the resonance frequency ω_o increases.
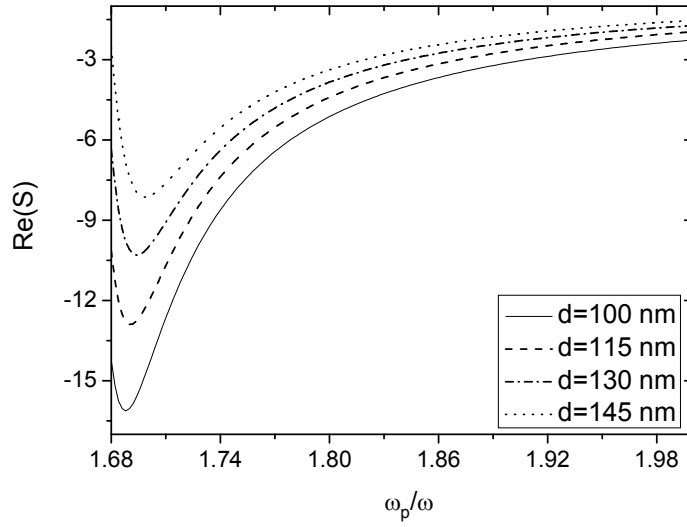
Fig. 3.5. The real part of the sensitivity of as a function of ω_p/ω for different thicknesses of the guiding layer for $\lambda = 1064$ nm, $\varepsilon_1 = \varepsilon_3 = 1.77$, $\mu_1 = \mu_3 = 1$, $\gamma = 0.012\omega_p$, $F = 0.58$, $\omega_0 = 0.4\omega_p$, and $\omega_p = 2\omega$.

.
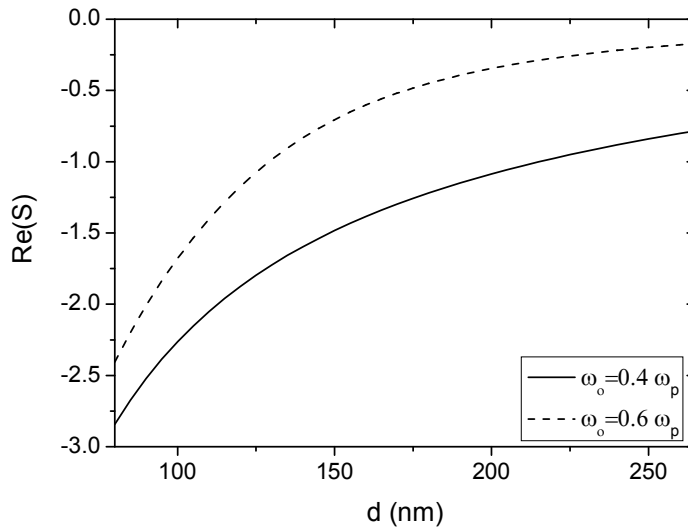
Fig. 3.6. The real part of the sensitivity as a function of d and ω_o for $\lambda = 1064$ nm, $\varepsilon_1 = \varepsilon_3 = 1.77$, $\mu_1 = \mu_3 = 1$, $\gamma = 0.012\omega_p$, $F = 0.58$, and $\omega_p = 2\omega$.

.

65
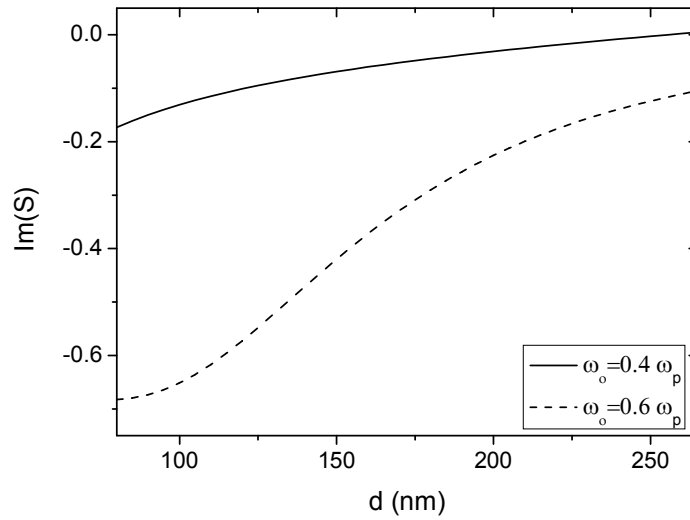
Fig.3.7. The imaginary part of the sensitivity of TM mode as a function of the thickness of the LHM layer for different values of resonance frequency ω_o for $\lambda = 1064$ nm, $\varepsilon_1 = \varepsilon_3 = 1.77$, $\mu_1 = \mu_3 = 1$, $\gamma = 0.012\omega_p$, $F = 0.58$, and $\omega_p = 2\omega$.

Figures 3.8 and 3.9 shows the real and imaginary parts of the sensitivity versus the LHM layer thickness for different values of F. The absolute value of the imaginary part of the sensitivity can be enhanced by decreasing F whereas the real part of the sensitivity, due to its high value, does not exhibit a remarkable change with F.
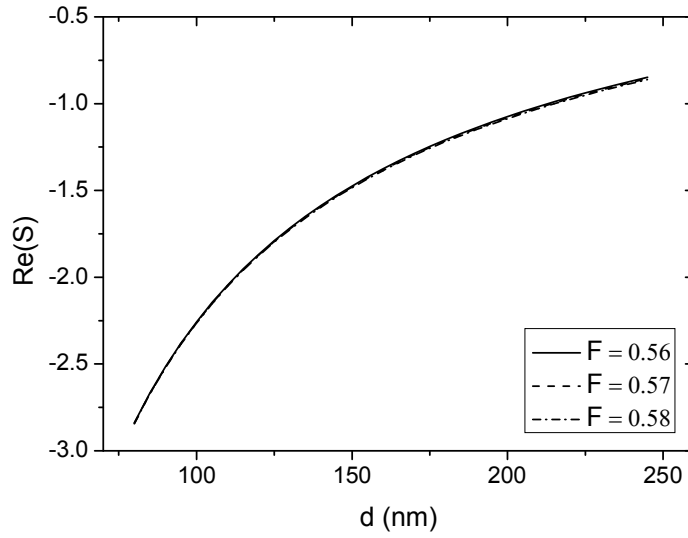
Fig.3.8. The real part of the sensitivity of the proposed sensor versus the thickness of the guiding layer for different values of the fractional area of the unit cell occupied by the split ring for $\lambda = 1064$ nm, $\varepsilon_1 = \varepsilon_3 = 1.77$, $\mu_1 = \mu_3 = 1$, $\gamma = 0.012\omega_\mathrm{p}$, $\omega_0 = 0.4\omega_p$, and $\omega_p = 2\omega$.
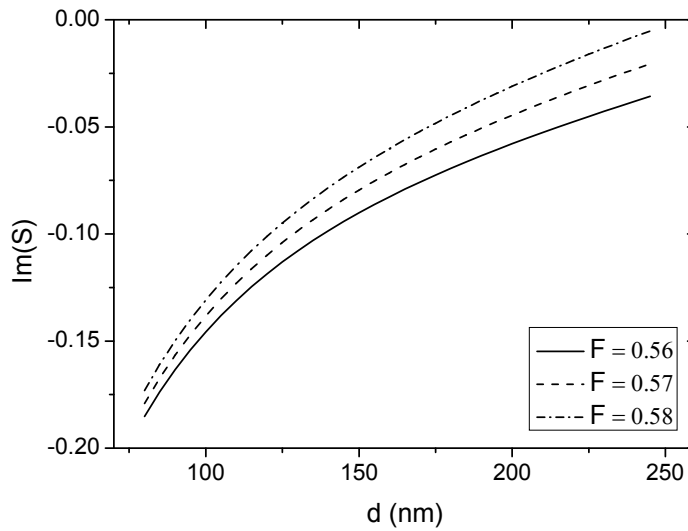
Fig. 3.9. The imaginary part of the sensitivity of the proposed sensor versus the thickness of the guiding layer for different values of the fractional area of the unit cell occupied by the split ring for $\lambda = 1064$ nm, $\varepsilon_1 = \varepsilon_3 = 1.77$, $\mu_1 = \mu_3 = 1$, $\gamma = 0.012\omega_\mathrm{p}$, $\omega_0 = 0.4\omega_p$, and $\omega_p = 2\omega$.

Figure 3.10 shows the variation of the real part of the sensitivity with the thickness d of the LHM layer for different values of cover refractive index. As expected, increasing the cover refractive index enhances the evanescent field into the cladding region, which in turn enhances the sensitivity of the sensor to changes in the index of the analyte.
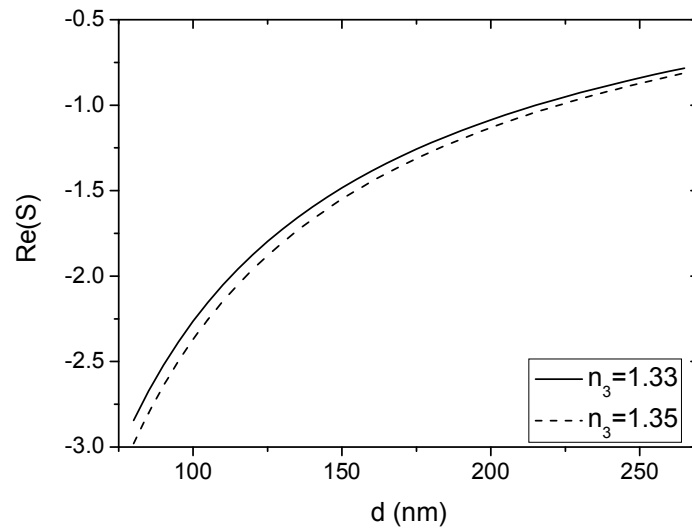
Fig. 3.10. The real part of the sensitivity of TM mode as a function of the thickness of the LHM layer for different values of cover refractive index for $\lambda = 1064$ nm, $\varepsilon_1 = \varepsilon_3 = 1.77$, $\mu_1 = \mu_3 = 1$, $\gamma = 0.012\omega_p$, $F = 0.58$, $\omega_0 = 0.4\omega_p$, and $\omega_p = 2\omega$.
.

Figure 3.11 shows the power confinement factor in the film layer Γ_f, the cladding layer Γ_c, and the substrate layer Γ_s as a function of thickness of the LHM layer for different values of γ. Due to the symmetric configuration assumed in the calculations, there is no cut-off thickness and therefore the size of the guiding layer can go to zero theoretically. The power distributions are in the expected shape. The power confinement factor within the film region increases as the thickness d increases at the expense of Γ_c and Γ_s. Due to the symmetric configuration assumed Γ_c and Γ_s are identical. The impact of γ on Γ_j is not very big. Increasing γ between $0.010\omega_p$ to $0.012\omega_p$ causes a little

enhancement in Γ_c and Γ_s. A well known feature appears in Fig. 3.11 which is the negative value of Γ_f. This is one of the main differences between negative index and positive index materials. In positive index materials, the Poynting's vector S always forms a right-handed set with the vectors E and H. Accordingly, S and the propagation vector k are in the same direction. However, this is not the case of LHMs in which S and k are in opposite directions.
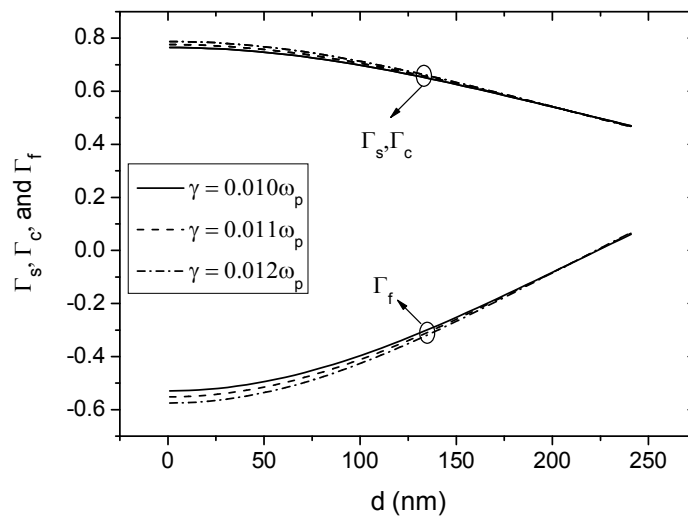
Fig. 3.11. The real part of confinement factors as a function of d and γ for $\lambda = 1064$ nm, $\varepsilon_1 = \varepsilon_3 = 1.77$, $\mu_1 = \mu_3 = 1$, $F = 0.58$, $\omega_0 = 0.4\omega_p$, and $\omega_p = 2\omega$.

Chapter four

# Metal-clad slab waveguide sensor

In this chapter, we assume a four-layer waveguide comprising a dielectric substrate, a metal layer, a LHM as a guiding layer, and a cladding which is the material to be detected. Such a structure is called metal-clad waveguide. Fresnel reflection coefficients are used to study the resonance dips at which the reflectance minimizes. Both the angular shift and the width of the resonances are presented and discussed.

4.1. Introduction

As mentioned in chapter 1, many attemps have been presented since the emergence of the slab waveguide sensors to improve the sensitivity. Among these attemps was the reverse symmetry design in which the refractive index of the substrate is takes to be less than that of the cladding [29,72-74]. Salamon et al. [75-78] proposed the coupled plasmon-waveguide resonance sensor. In 2005, metal-clad waveguide sensors have been proposed and investigated in details [74]. In this chapter we present metal-clad waveguide sensor using a LHM core layer.

4.2. Structure analysis

Figure 4.1 shows a schematic diagram of the planar metal-clad waveguide configuration. It consists of four layers with LHM film layer of thickness d_3 occupies the region $d_2 < z < d_2+d_3$, which is characterized by an electric permittivity ε_3 and magnetic permeability μ_3, given by Eqs. (2.1, 2.2).

A metal layer (silver or gold) occupies the region $0 < z < d_2$ and characterized by ε_2 and μ_2. The metal and LHM layers are sandwiched between an aqueous superstrate (ε_4, μ_4) and a dielectric substrate (ε_1, μ_1).
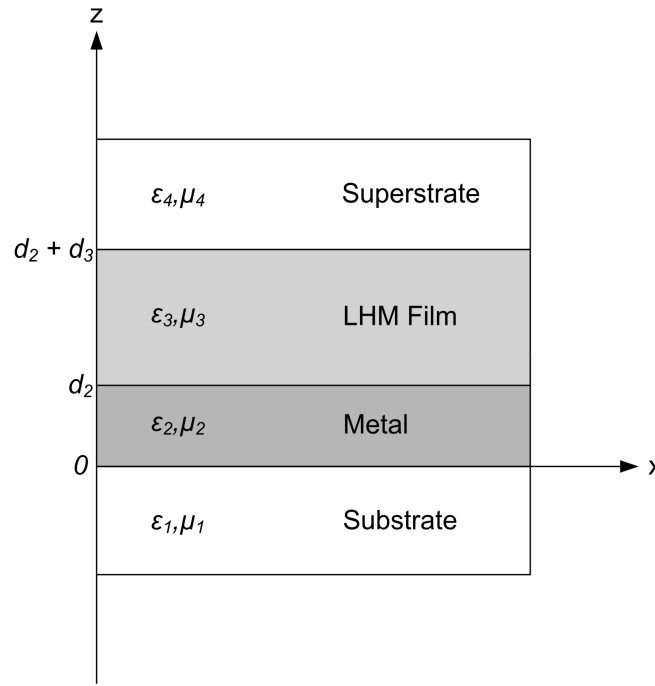
Fig. 4.1. A metal-clad waveguide structure configuration.

4.3. Fresnel reflection coefficients

Slab waveguides sensors are operated in two configurations. In the first one, the change in the effective refractive index of the guided mode is used to detect the changes in the index of an analyte. In the second configuration such as metal-clad waveguide sensors, the structure is operated in reflection mode in which the waveguide structure is illuminated from below and the reflected beam is received by a detector. The incidence angle is varied and the reflected intensity is measured as a function of the angle of incidence. This is due to the fact that the guided light in the guiding layer is strongly attenuated over a short distance due to the lossy metal layer and therefore is hardly measurable. Measuring the reflectance versus the incidence angle usually results in a chart

containing a clear dip at which the reflectance approaches zero at an angle of incidence called the resonance angle. The reflectance as a function of the incidence angle can be calculated using Fresnel's reflection laws. From section 1.2.6., the reflectance from a layered structure can be calculated using Fresnel's reflection laws. For TE-mode, the reflectance from three-layer is given by

$$R_{123} = |r_{123}|^2 = \left| \frac{r_{12} + r_{23} \exp(2i\beta_2 d_2)}{1 + r_{12}r_{23} \exp(2i\beta_2 d_2)} \right|^2 , \qquad (4.1)$$

$$r_{i,j} = \frac{\mu_j \beta_i - \mu_i \beta_j}{\mu_j \beta_i + \mu_i \beta_j} , \qquad (4.2)$$

$$\beta_j = \pm k_o \sqrt{\varepsilon_j \mu_j - N^2} , \qquad (4.3)$$

where $r_{i,j}$ is the amplitude reflection coefficient between layers i and j, d_2 is the thickness of layer 2, β_i is the normal wavevector component in medium i, μ_j is the magnetic permeability of medium j, ε_j is the electric permittivity of medium j, and N is the effective refractive index. The effective refractive index is given by

$$N = \frac{k_x}{k_o} = n_j \sin(\Theta_j) , \qquad (4.4)$$

where Θ_j (j = 1, 2, 3, 4) represents any of the individual angles of incidence. The reflectance from a four layer structure shown in Fig. 4.1. is therefore given by

$$R_{1234} = |r_{1234}|^2 = \left| \frac{r_{12} + r_{234} \exp(2i\beta_2 d_2)}{1 + r_{12}r_{234} \exp(2i\beta_2 d_2)} \right|^2 , \qquad (4.5)$$

where r_{234} has the same form given by Eq. (4.1) with the appropriate indices. The relations for TM-mode can be obtained if μ in the last equations is replaced with ε.

4.4. Dispersion relation

For TE-mode, the solution of Helmholtz equation for the time harmonic electric field is given by

$$\vec{E} = \begin{cases} a_4^+ e^{i(k_x x + \beta_4 z)} \ \hat{y} & \text{Superstrate Layer} \\ \left(a_3^+ e^{i(k_x x + \beta_3 z)} + a_3^- e^{i(k_x x - \beta_3 z)} \right) \hat{y} & \text{Film Layer} \\ \left(a_2^+ e^{i(k_x x + \beta_2 z)} + a_2^- e^{i(k_x x - \beta_2 z)} \right) \hat{y} & \text{Metal Layer} \\ a_1^- e^{i(k_x x - \beta_1 z)} \ \hat{y} & \text{Substrate Layer} \end{cases} \quad , \quad (4.5)$$

where $a_j^{+,-}$ (j=1, 2, 3, 4) are the amplitudes of the up- and down going waves in the individual media.

The tangential nonzero components of the magnetic field can be obtained using Maxwell's relations

$$H_x = \begin{cases} -a_4^+ \dfrac{\beta_4}{\omega \mu_4} e^{i(k_x x + \beta_4 z)} & \text{Superstrate Layer} \\ \dfrac{\beta_3}{\omega \mu_3} \left(-a_3^+ e^{i(k_x x + \beta_3 z)} + a_3^- e^{i(k_x x - \beta_3 z)} \right) & \text{Film Layer} \\ \dfrac{\beta_2}{\omega \mu_2} \left(-a_2^+ e^{i(k_x x + \beta_2 z)} + a_2^- e^{i(k_x x - \beta_2 z)} \right) & \text{Metal Layer} \\ a_1^- \dfrac{\beta_1}{\omega \mu_1} e^{i(k_x x - \beta_1 z)} & \text{Substrate Layer} \end{cases} \quad , (4.6)$$

where $\beta_j = k_0 (\varepsilon_j \mu_j - N^2)^{1/2}$. Applying the boundary conditions for the TE-polarized light, six equations are obtained and can be written in the form [74]

$$A \vec{\psi} = \vec{0}, \quad (4.7)$$

with

$$\vec{\psi} = \left\{ a_4^+, a_3^+, a_3^-, a_2^+, a_2^-, a_1^- \right\}, \quad (4.8)$$

and

$$A = \begin{bmatrix}
e^{i\beta_4(d_2+d_3)} & -e^{i\beta_3(d_2+d_3)} & -e^{-i\beta_3(d_2+d_3)} & 0 & 0 & 0 \\[4pt]
\dfrac{\beta_4}{\mu_4}e^{i\beta_4(d_2+d_3)} & -\dfrac{\beta_3}{\mu_3}e^{i\beta_3(d_2+d_3)} & \dfrac{\beta_3}{\mu_3}e^{-i\beta_3(d_2+d_3)} & 0 & 0 & 0 \\[4pt]
0 & e^{i\beta_3 d_2} & e^{-i\beta_3 d_2} & -e^{i\beta_2 d_2} & -e^{-i\beta_2 d_2} & 0 \\[4pt]
0 & \dfrac{\beta_3}{\mu_3}e^{i\beta_3 d_2} & -\dfrac{\beta_3}{\mu_3}e^{-i\beta_3 d_2} & -\dfrac{\beta_2}{\mu_2}e^{i\beta_2 d_2} & \dfrac{\beta_2}{\mu_2}e^{-i\beta_2 d_2} & 0 \\[4pt]
0 & 0 & 0 & 1 & 1 & 1 \\[4pt]
0 & 0 & 0 & \dfrac{\beta_2}{\mu_2} & -\dfrac{\beta_2}{\mu_2} & \dfrac{\beta_1}{\mu_1}
\end{bmatrix}$$

(4.9)

where d_2 and d_3 are the metal and film thicknesses, respectively. The determinant of this set must be zero for nontrivial solutions to exist, which leads to the dispersion equation of TE-polarized light

$$2\beta_3 d_3 + \Phi_{3,4} + \Phi_{3,2,1} = \pm 2\pi m, \tag{4.10}$$

where

$$\Phi_{3,4} = 2\arctan\left(i\frac{\mu_3 \beta_4}{\mu_4 \beta_3}\right),$$

$$\Phi_{3,2,1} = 2\arctan\left(i\frac{(1-r_{3,2})}{(1+r_{3,2})}\frac{(1-r_{2,1}e^{2i\beta_2 d_2})}{(1+r_{2,1}e^{2i\beta_2 d_2})}\right),$$

$$\beta_j = \pm k_o\sqrt{\varepsilon_j \mu_j - N^2}, \; j=1,2,3, \; and \; 4$$

$$r_{3,2} = \frac{\mu_2 \beta_3 - \mu_3 \beta_2}{\mu_2 \beta_3 + \mu_3 \beta_2},$$

$$r_{2,1} = \frac{\mu_1 \beta_2 - \mu_2 \beta_1}{\mu_1 \beta_2 + \mu_2 \beta_1},$$

$m = 0, 1, 2, \ldots$ is the mode order. $\Phi_{3,4}$ and $\Phi_{3,2,1}$ are the phase shifts the wave undergoes upon reflected at the film-cladding and the film-metal interfaces, respectively.

To obtain the relations of TM-polarized light we replace μ_1, μ_2, μ_3, and μ_4 by ε_1, ε_2, ε_3, and ε_4, respectively, in the above set of equations.

4.5. Numerical results

Lossless LHM only represents an ideal case. In all LHM practical designs, a lossy material with negative parameters was obtained .Thus LHM material with absorption coefficient seems to be more realistic. Moreover, LHMs with minimal absorption coefficient have been reported to focus light onto an area smaller than a square wavelength in near fields [79]. This behavior is attributed the amplification of evanescent waves caused by LHMs. Thus, in our calculations, we assume the LHM guiding layer to have an electric permittivity and a magnetic permeability of the form $\varepsilon_3 = \varepsilon_{3r} + i\varepsilon_{3i}$ and $\mu_3 = \mu_{3r} + \mu_{3i}$, respectively. He-Ne laser beam of $\lambda = 632.8$ nm is assumed. The cladding is considered to be water ($n_4 = 1.33$) and the substrate is glass ($n_1 = 1.517$).

Figures 4.2 and 4.3 show the reflectance of TM-polarized light from a metal-clad waveguide as a function of the incidence angle (Θ_1) for two different values of the LHM film thickness. In Fig. 4.2, we used silver cladding whereas gold cladding was used in Fig. 4.3. When $d_3 = 0$, the reflectance dip represents the surface plasmon resonance (SPR) mode. For film thickness > 0, the reflectance dip represent the metal-clad waveguide configuration.
It is clear that a sharper dip is obtained in the presence of 350 nm LHM guiding layer between the metal and cladding layers. This is an advantage of metal-clad waveguide configurations over SPR structures for sensing applications. It is well-known that the principle of operation of reflection mode optical sensor is based on measuring the angular shift of the reflectance dip when the refractive index of the cladding changes. Therefore, when the dip is sharper the reading is easier and more accurate.

The choice of the metal plays a significant role in the reflectance dip sharpness. The losses in metal-clad waveguide configuration is strongly dependent on the imaginary part of metal permittivity ($\varepsilon_2^{"}$). The larger the value of the imaginary part of ε_2 leads to a broader dip [80,81]. Accordingly, the dip of the silver-clad waveguide (Fig. 4.2) is much sharper than that of gold-clad waveguide (Fig. 4.3) since $\varepsilon_2^{"}(Au) > \varepsilon_2^{"}(Ag)$.
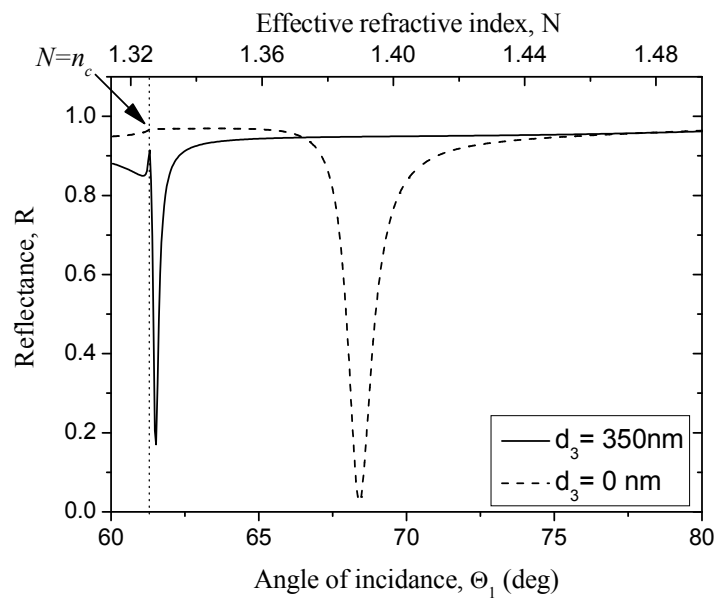
Fig. 4.2. Calculated reflectance for TM-mode light reflected from a silver-clad waveguide with and without a LHM film layer for d_2= 60nm, λ = 632.8nm, ε_1 = 2.3, ε_2 = -16+i0.52, ε_3 = -4+i0.001, ε_4=1.77, μ_1 = 1, μ_2 = 1, μ_3 = -2.4+i0.001, and μ_4 = 1.

Fig. 4.3. Calculated reflectance for TM-mode light reflected from a gold-clad waveguide with and without a LHM film layer for $d_2 = 60$nm, $\lambda = 632.8$nm, $\varepsilon_1 = 2.3$, $\varepsilon_2 = -10.22+i0.96$, $\varepsilon_3 = -4+i0.001$, $\varepsilon_4 = 1.77$, $\mu_1 = 1$, $\mu_2 = 1$, $\mu_3 = -2.4+i0.001$, and $\mu_4 = 1$.

In Figs. 4.4 calculated reflectance from silver-clad waveguide (a) and gold-clad waveguide (b) with three different thicknesses of the metal cladding are presented. From the figures its clear that the thickness of the metal layer is important for the shape and depth of the reflectance dip. For both the silver-clad waveguide and gold-clad waveguide the position and the shape of the reflectance dip are change with metal thickness. At a metal thickness of 40 nm the reflectance approaches zero, which is defined as the optimum metal thickness. As the metal layer gets thinner, the reflectance dip gets deeper and sharper.
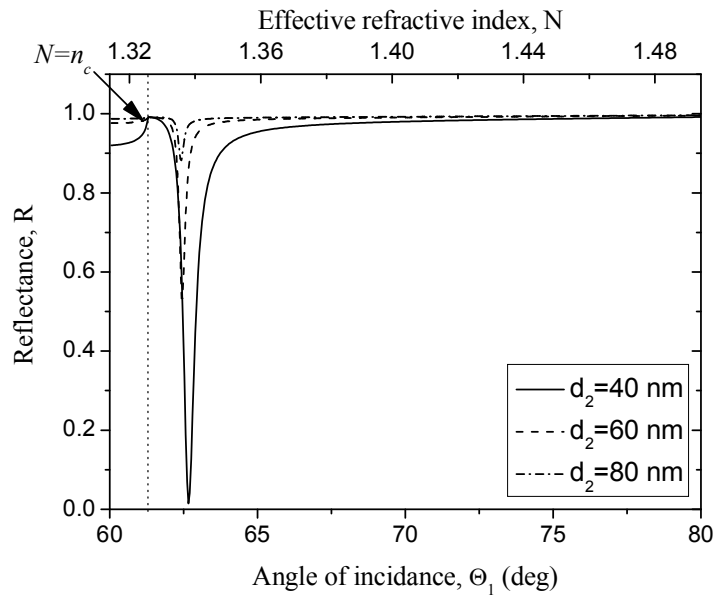
(a)
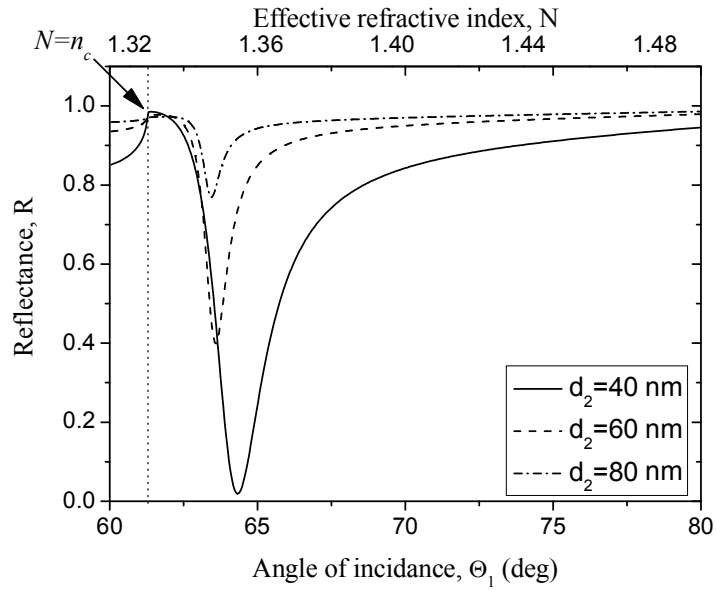
(b)

Fig. 4.4. Calculated reflectance for TE-mode light reflected from (a) a silver-clad waveguide and (b) a gold-clad waveguide for different values of metal thickness for $d_3 = 250$nm, $\lambda = 632.8$nm, $\varepsilon_1 = 2.3$, $\varepsilon_2 = -16+i0.52$ (silver), $\varepsilon_2 = -10.22+i0.96$ (gold), $\varepsilon_3 = -4+i0.001$, $\varepsilon_4 = 1.77$, $\mu_1 = 1$, $\mu_2 = 1$, $\mu_3 = -3+i0.001$, and $\mu_4 = 1$.

It is very important when proposing a metal-clad waveguide configuration with a LHM film for sensor applications to study the effect of the parameters of the LHM layer on the reflectance curves. In Fig. 4.5 we study the effect of the LHM layer thickness on these curves. As can be seen from Fig. 4.5 (a) and (b) increasing the thickness of the LHM layer shifts the reflectance dip towards lower incidence resonance angles for both silver and gold metals.

(a)

(b)

Fig. 4.5. Calculated reflectance for TE-mode light reflected from (a) a silver-clad waveguide and (b) a gold-clad waveguide for different values of LHM film thickness for d_2 = 40nm, λ = 632.8nm, ε_1 = 2.3, ε_2 = -16+i0.52 (silver), ε_2 = -10.22+i0.96 (gold), ε_3 = -4+i0.001, ε_4 = 1.77, μ_1 = 1, μ_2 = 1, μ_3 = -3+i0.001, and μ_4 = 1.
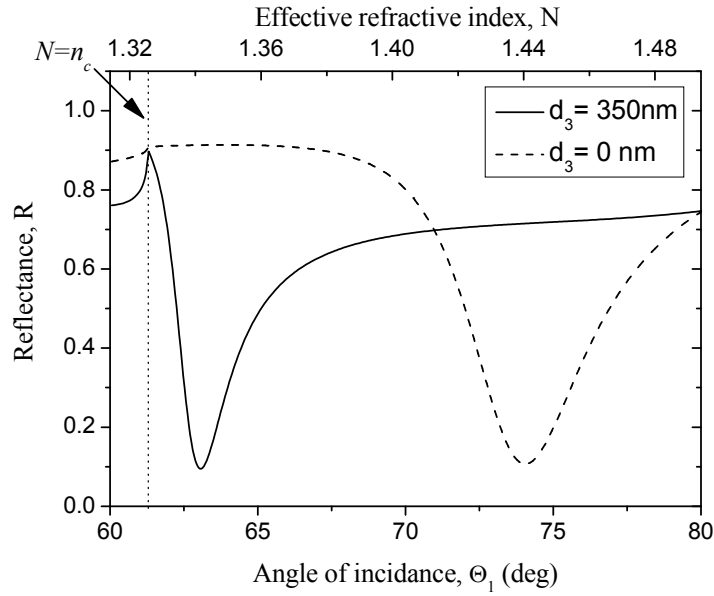
We also investigate the effect of the electric permittivity (ε_3) and the magnetic permeability (μ_3) of the LHM film on the reflectance curves. As the absolute value of the real part of both ε_3 and μ_3 increases, the reflectance dip become sharper and the angular position of the resonance dip decreases as shown in Figs. 4.6 and 4.7.

(a)

(b)

Fig. 4.6. Calculated reflectance for TE-mode light reflected from (a) a silver-clad waveguide and (b) a gold-clad waveguide for different values of permittivity of the LHM film for $d_2 = 40$nm, $d_3 = 250$nm, $\lambda = 632.8$nm $\varepsilon_1 = 2.3$, $\varepsilon_2 = -16 + i0.52$ (silver), $\varepsilon_2 = -10.22 + i0.96$ (gold), $\varepsilon_4 = 1.77$, $\mu_1 = 1$, $\mu_2 = 1$, $\mu_3 = -3 + i0.001$, and $\mu_4 = 1$.
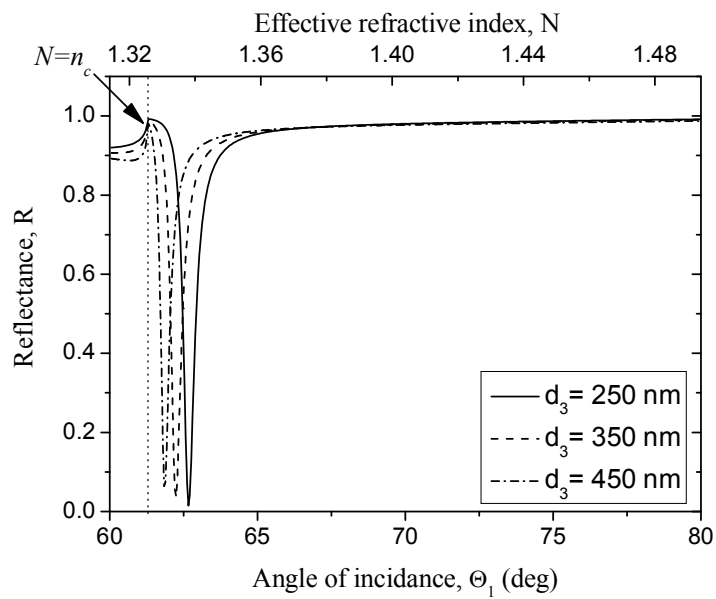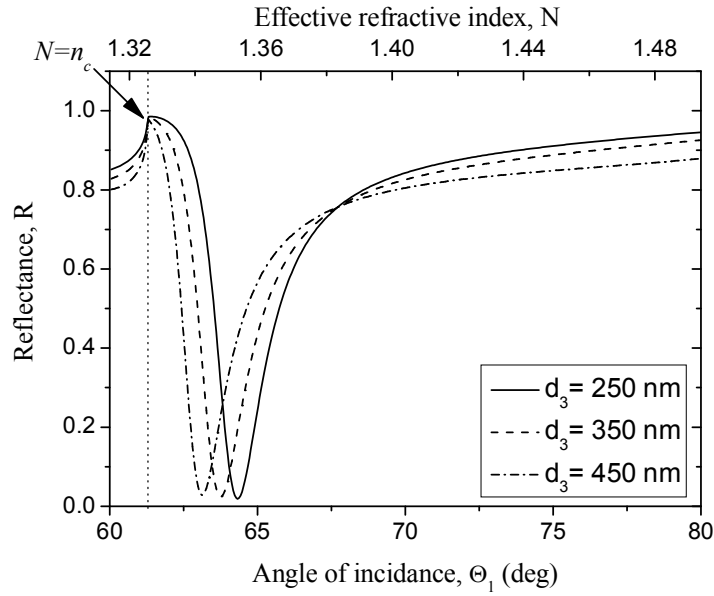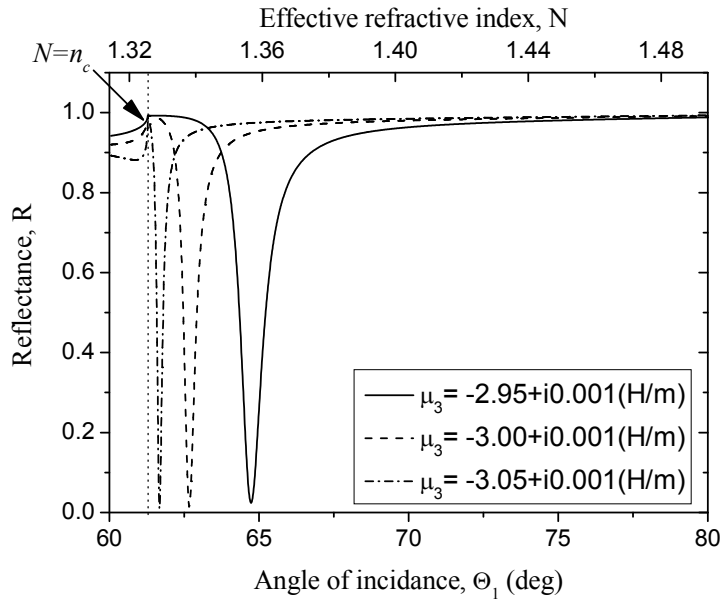
(a)
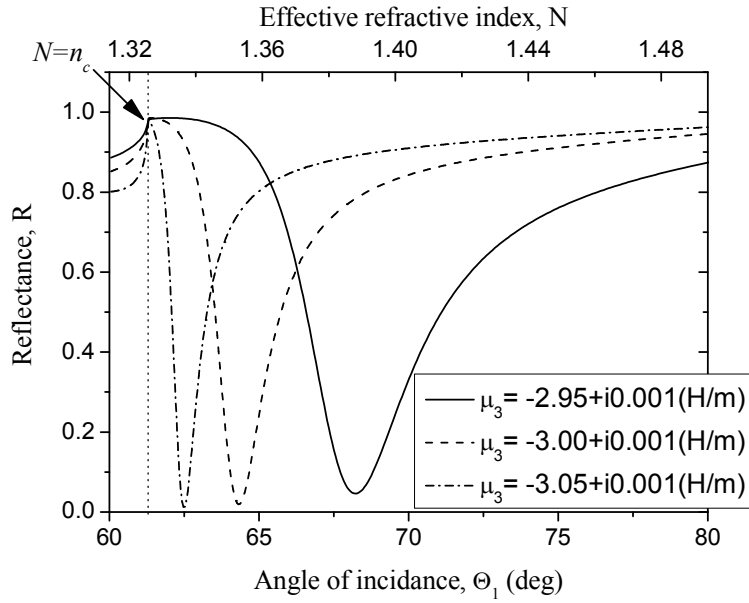
(b)

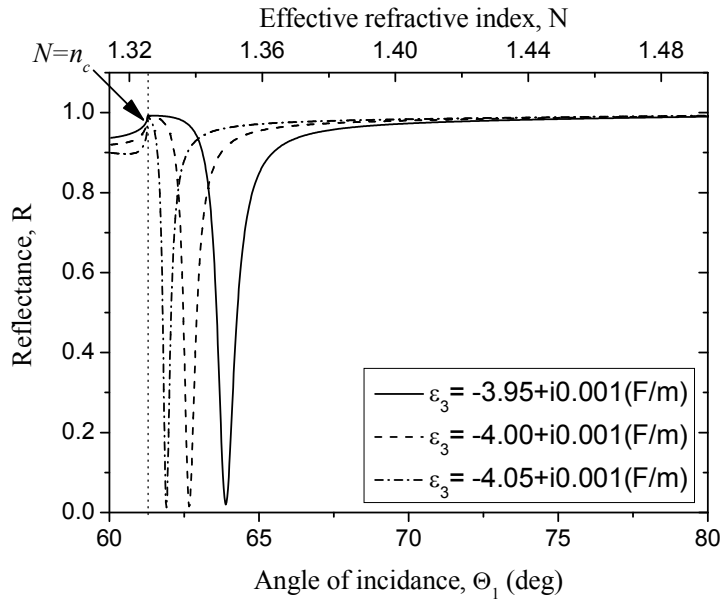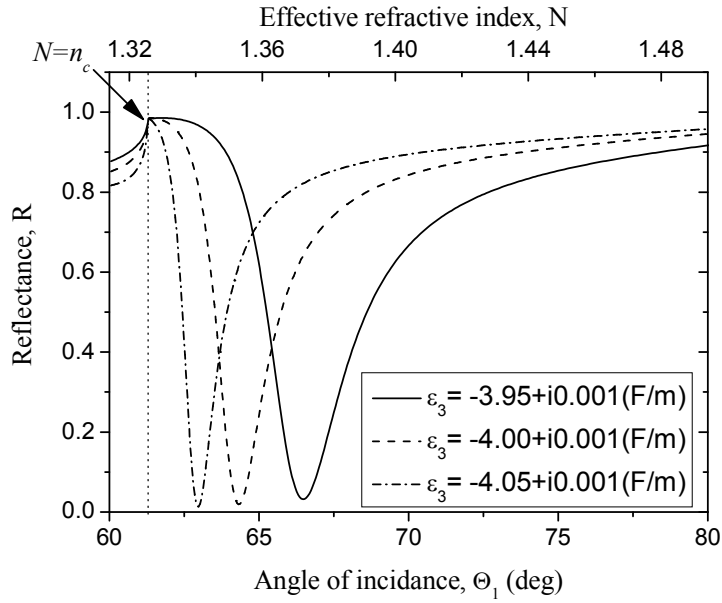Fig. 4.7. Calculated reflectance for TE-mode light reflected from (a) a silver-clad waveguide and (b) a gold-clad waveguide for different values of permeability of the LHM film for d_2 = 40nm, d_3 = 250nm, λ = 632.8nm ε_1 = 2.3, ε_2 = -16+i0.52 (silver), ε_2 =-10.22+i0.96 (gold), ε_3 = -4+i0.001, ε_4 = 1.77, μ_1 = 1, μ_2 = 1, and μ_4 = 1.

In Fig. 4.8 the pairs of reflectance curves illustrate the shifts in dip position due to small changes in the cover refractive index (n_4). The width of the dips are much larger for the SPR modes compared with the waveguide dips, and the dips approach to zero in the metal-clad waveguide modes.
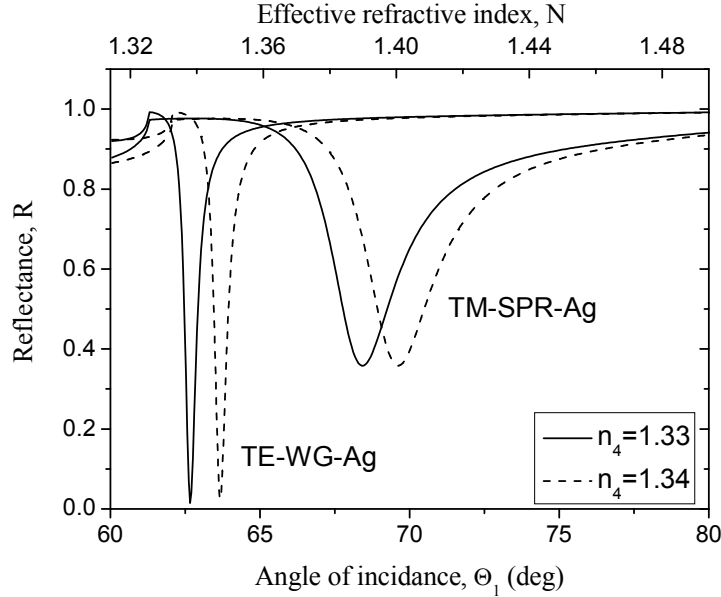
Fig. 4.8. Calculated reflectance for a silver-clad waveguide for different values of n_4 for d_2=40nm, d_3=250nm, λ=632.8nm, ε_1 = 2.3, ε_2 = -16+i0.52, ε_3 = -4+i0.001, ε_4 = 1.77, μ_1 = 1, μ_2 = 1, μ_3 = -3+i0.001, and μ_4 = 1.

The reflectance curves of a TM-polarized light from a silver-cladding waveguide is plotted for different values of n_4 in Fig. 4.9.

For n_4 = 1.33, the critical angle and the reflectance dip are barely separated and the limiting parameter of the detection range is the thickness of the waveguide film. As n_4 increases the reflectance dip gets broader.
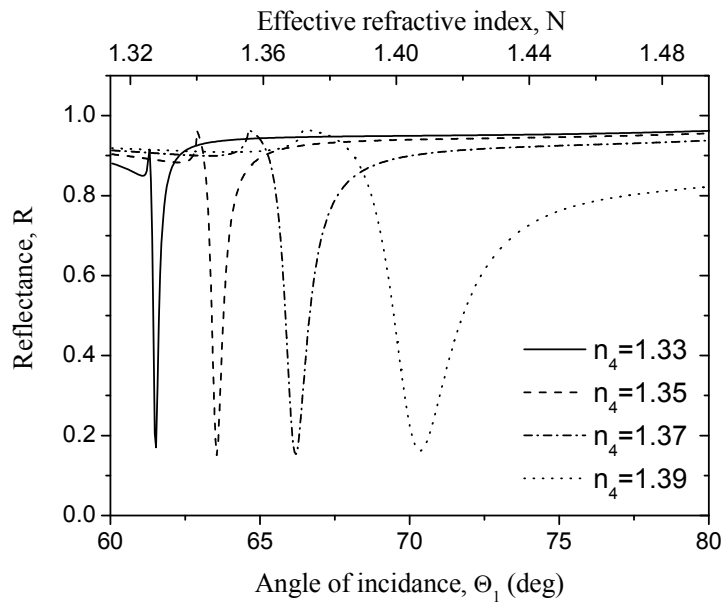
Fig. 4.9. Calculated reflectance for TM-mode light reflected from a silver-clad waveguide for different values of n_4 for $d_2 = 40$ nm, $d_3 = 250$ nm, $\lambda = 632.8$ nm, $\varepsilon_1 = 2.3$, $\varepsilon_2 = -16 + i0.52$, $\varepsilon_3 = -4 + i0.001$, $\varepsilon_4 = 1.77$, $\mu_1 = 1$, $\mu_2 = 1$, $\mu_3 = -2.4 + i0.001$, and $\mu_4 = 1$.

Chapter five

Conclusion

In this thesis, analyzed a slab waveguide for sensing purposes has been analyzed. a three layer slab waveguide sensor and a dip-type metal-clad waveguide sensor, each sensor consisting of a LHM as a guiding layer, have been studied.

The three-layer slab waveguide sensor has been studied for two cases, TE- and TM- modes.

In order to optimize the proposed structure, it is significant to study the sensitivity dependence on the different parameters of the LHM guiding layer.

In the case of TE-mode, the following observations are obtained:

- The sensitivity is negative and has a peak at a specific value of the guiding layer thickness (d). The film power is also negative.

- The absolute value of the sensitivity decays towards lower values for high values of d due to the high field confinement.

- The absolute values of the real and imaginary parts of the sensitivity increase as γ decreases. The confinement factor for the cladding layer is enhanced with decreasing γ. Therefore, γ should be as low as possible.

- The Re(S) and Im(S) exhibit different behaviors with F. In contrary to Im(S), the absolute value of Re(S) increases with increasing F for a given value of d.

- The higher the value of F, the more the fractional power in the cladding which leads to a higher sensitivity.

For the case of TM-mode, we consider a symmetric slab waveguide and we study the sensitivity as a function of ω_p/ω for the range $1.68 < \omega_p/\omega < 2$ (in GHz) in which the real parts of ε_2 and μ_2 are both negative to make sure that the guiding layer is made of a left-handed material. Also we study the sensitivity as a function of thickness of the guiding layer and γ. The following remarks have been observed:

- The real part of the effective refractive index is much more sensitive to variations of the cladding index than the imaginary part. Accordingly, the Re(S) is about 26.77 times the Im(S) for a specific configuration.

- The sensitivity of the imaginary part of the effective index can be slightly improved with increasing γ, whereas the Re(S), due to its high value, is barely affected with changing γ in the considered range of γ.

- Both the real and imaginary parts of S show the same behavior with the thickness of the guiding LHM layer. The absolute value of both parts of the sensitivity maximizes for low values of d and decays with increasing the thickness.

- The most important feature is that through proper choice of ω_p/ω and d, the Re(S) may reach a value of order -16 which means the enhancement factor of the sensitivity of the proposed sensor could be of order 32.

We also study the Fresnel reflection coefficients for TE- and TM-modes from metal-clad waveguide. The operation of sensing is more accurate if the reflectance dip is sharper since the reading of the angular shift becomes easier. A number of interesting features can be observed:

- A sharper dip is obtained in the presence of 350 nm LHM guiding layer between the metal and the cladding layer. This is an advantage of metal-clad waveguide configuration over SPR structure for sensing applications.

- The larger the value of the imaginary part of ε_2 leads to a broader dip since the losses in metal-clad waveguide configuration is strongly dependent on the imaginary part of metal permittivity (ε_2''). As a result, the dip of the silver-clad waveguide is much sharper than that of gold-clad waveguide.

- The position and shape of the reflectance dip change with metal thickness, the optimum metal thickness is found to be 40 nm at which the reflectance approaches zero. Decreasing d_2 increases the minimum reflectance and the dip becomes sharper.

- As the real part of both ε_3 and μ_3 increases, the reflectance dip become sharper and the angular position of the resonance dip decreases.

References

[1] F. Pedrotti and L. Pedrotti, Introduction to Optics, 2nd edition, Prentice Hall, New Jersey, 1993.

[2] H. Fujiwara, Spectroscopic Ellipsometry, Principles and Applications, 1st edition, Wiley-Interference, England, 2007.

[3] E. Hecht, Optics, 4th edition, Addison Wesley, San Francisco, 2002.

[4] D. Griffiths, Introduction to Electrodynamics, 3rd edition, Prentice Hall, New Jersey, 1999.

[5] J. Jackson, Classical Electrodynamics, 3rd edition, Wiley-Interference, New York, 1999.

[6] P. Markoš and C. Soukoulis, Wave Propagation, From Electrons to Photonic Crystals and Left-Handed Materials, 1st edition, Princeton University Press, New Jersey, 2008.

[7] F. Jenkins and H. White, Fundamentals of Optics, 4th edition, McGraw Hill, New York, 2001.

[8] B. Saleh and M. Teich, Fundamentals of Photonics, 2nd edition, Wiley-Interference, New Jersey, 2007.

[9] M. Born and E. Wolf. Principles of Optics, electromagnetic theory of propagation, interference and diffraction of light, 7th edition, Cambridge University Press, Cambridge, 1999.

[10] P. Banerjee and T. Poon, Principles of Applied Optics, 1st edition, IRWIN, Boston, 1991.

[11] R. Guentther, Modern Optics, 1st edition, Wiley-Interference, Canada, 1990.

[12] G. Fowles, Introduction to Modern Optics, 2nd edition, Dover Publications, New York, 1975.

[13] A. Ghatak and K. Thyagarajan, Introduction to Fiber Optics, 1st edition, Cambridge University Press, New Delhi, 2002.

[14] K. Okamoto, Fundamentals of Optical Waveguides, 2nd edition, Elsevier, Amsterdam, 2006.

[15] Chin-Lin Chen, Foundations for Guided-Wave Optics, Wiley-Interference, New Jersey, 2007.

[16] C. Yeh and F. Shimabukuro, The Essence of Dielectric Waveguides, 1st edition, Springer, New York, 2008.

[17] R. Serway and J. Jewett, Physics for Scientist and Engineers, 6th edition, Brooks/Cole Thomson Learning, Belmont, 2004.

[18] K. Tiefenthaler and W. Lukosz, Sensitivity of grating couplers as integrated-optical chemical sensors, J. Opt. Soc. Am. B, Vol. 6 (2), pp. 209–220, 1989.

[19] O. Parriaux and P. Dierauer, Normalized expressions for the optical sensitivity of evanescent wave sensors, Opt. Lett., Vol. 19, pp. 508–510, 1994.

[20] R. Horvath, N. Skivesen, and Pederson H., Measurement of guided light-mode intensity: an alternative waveguide sensing principle, App. Phys. Lett., Vol. 84, pp. 4044–4046, 2004.

[21] S. Taya and T. El-Agez, Comparing optical sensing using slab waveguides and total internal reflection ellipsometry, Turk. J. Phys., Vol. 35, pp. 31-36, 2011.

[22] T. El-Agez and S. Taya, Theoretical spectroscopic scan of the sensitivity of asymmetric slab waveguide sensors, Optica Applicata, Vol. 41(1), pp. 89-95, 2011.

[23] S. Taya, M. Shabat, and H. Khalil, Enhancement of Sensitivity in optical sensors using left-handed materials, Optik, Vol. 120, pp. 504-508, 2009.

[24] S. Taya, M. Shabat, and H. Khalil, Nonlinear Planar Asymmetrical Optical Waveguides for Sensing Applications, Optik, Vol. 121, pp. 860-865, 2010.

[25] S. Taya, M. Shabat, H. Khalil, and D. Jäger, Theoretical Analysis of TM Nonlinear Asymmetrical Waveguide Optical sensors, Sens. Actuat. A, Vol. 147, pp. 137-141, 2008.

[26] M. Shabat, H. Khalil., S. Taya, and M. Abadla, Analysis of the sensitivity of self-focused nonlinear optical evanescent waveguide sensors, Int. J. Optomechatronics, Vol. 1, pp. 284-296, 2007.

[27] H. Khalil, M. Shabat, S. Taya., and M. Abadla., Nonlinear optical waveguide structure for sensor application: TM case, Int. J. Modern Phys. B, Vol. 21(30), pp. 5075-5089, 2007.

[28] S. Taya and T. El-Agez, Reverse symmetry optical waveguide sensor using plasma substrate, J. Opt., Vol. 13, pp. 075701, 2011.

[29] R. Horvath, H. Pederson, and N. Larsen, Demonstration of reverse symmetry waveguide sensing in aqueous solutions, App. Phys. Lett., Vol. 81, pp. 2166–2168, 2002.

[30] D. kumar and V. Singh, Theoretical modeling of a nonlinear asymmetric metal-clad planar waveguide based sensor, Optik, 2011, doi:10.1016/j.ijleo.2010.12.031.

[31] S. Ramakrishna, Physics of negative refractive index materials, Rep. Prog. Phys., Vol. 68, pp. 449–521, 2005.

[32] V. Veselago, L. Braginsky, V. Shklover, and C. Hafner, Negative Refractive Index Materials, J. Comput. Theor. Nanosci., Vol. 3(2), pp. 1-30, 2006.

[33] D. Smith and N. Kroll, Negative Refractive Index in Left-handed materials. phys. Rev. lett., Vol. 85, pp. 2933-2936, 2000.

[34] R. Walser, Metamaterials: An introduction. In W. S. Weiglhofer and A. Lakhtakia, editors, Introduction to Complex Mediums for Optics and Electromagnetic, volume PM123. SPIE Press, Bellingham, WA, 2003.

[35] G. Eleftheriades and K. Balmain, Negative-Refraction Metamaterials, Wiley Interference, 2005, ISBN: 0-471-60146-3.

[36] S. Ramakrishna and T. Grzegorczyk, Physics and Applications of Negative Refractive Index Materials, CRC press, ISBN: 9780819473998.

[37] V. Veselago, The electrodynamics of substance with simultaneously negative index values of ε and μ, Sov. Phys. Usp., Vol. 10, pp. 509-514, 1968.

[38] A. Sarychev and V. Shalaev, Electrodynamics of Metamaterials, World Scientific, 2007, ISBN: 981-02-4245-X.

[39] W. Cai and V. Shalaev, Optical Metamaterials, Springer, 2010, ISBN: 978-1-4419-1150-6.

[40] T. Cui, D. Smith, and R. Liu, Metamaterials: Theory, Design, and Applications, Springer, 2010, ISBN: 978-1-4419-0572-7.

[41] J. Pendry, A. Holden, W. Stewart, and I. Youngs, Extremely low frequency plasmons in metallic mesostructures. Phys. Rev. Lett., Vol. 76(25), pp. 4773–4776, 1996.

[42] J. Pendry, A. Holden, D. Robbins, and W. Stewart, Low frequency plasmons in thin-wire structures. J. Phys.: Condens. Matter, Vol. 10, pp. 4785–4809, 1998.

[43] D. R. Smith, Willie J. Padilla, D. C. Vier, S. C. Nemat-Nasser, and S. Schultz, Composite medium with simultaneously negative permeability and permittivity. Phys. Rev. Lett., Vol. 84(18), pp. 4184–4187, 2000.

[44] R. A. Shelby, D. R. Smith, and S. Schultz, Experimental verification of a negative index of refraction. Science, Vol. 292, pp. 77–79, 2001.

[45] J. Kong, Electromagnetic wave interaction with stratified negative isotropic media, Progress in Electromagnetic research, Vol. 35, pp. 1-52, 2002.

[46] N. Engheta, Metamaterials with negative permittivity and permeability: background, salient features, and new trends, IEEE MTT_S Int. Microwave Symp. Digest, Vol. 1, pp. 187, 2003.

[47] W. Chew, Some reflections on double negative materials, Progress in Electromagnetic research, Vol. 51, p, 1, 2005.

[48] C. Sabah, G. Ogucu, and S. Uckun, Reflected and transmitted powers of electromagnetic wave through a double-negative slab, J. Optoelectronics and Advanced Materials, Vol. 8, pp. 1925, 2006.

[49] C. Sabah and S. Uckun, Electromagnetic wave propagation through frequency-dispersive and lossy double-negative slab, Optoelectronics Review, Vol. 15, pp. 133, 2007.

[50] S. Tretyakov, Meta-material with wide-band negative permittivity and permeability, Microwave and Optical Technology Letters, Vol. 31, pp. 163, 2001.

[51] C. Caloz, C. Chang, and T. Itoh, Full-wave verification of the fundamental properties of left-handed materials in waveguide configuration, Journal of Applied Physics, Vol. 90, pp. 5483, 2001.

[52] K. Guven and E. Ozbay, Near field imaging in microwave regime using double layer split-ring resonator based metamaterials, Opto-Electron. Review, Vol. 14, pp. 213, 2006.

[53] J. B. Pendry, Negative refraction makes a perfect lens. Phys. Rev. Lett., Vol. 85, pp. 3966–3969, 2000.

[54] W. Cai, D. Genov, and V. Shalaev, Superlens based on metal-dielectric composites. Phys. Rev. B, Vol. 72, pp. 193101, 2005.

[55] A. Grbic and G. Eleftheriadesm, Overcoming the diffraction limit with a planar left-handed transmission-line lens. Phys. Rev. Lett., Vol. 92, pp. 117403, 2004.

[56] N. Fang, H. Lee, C. Sun, and X. Zhang, Subdiffraction-limited optical imaging with a silver superlens. Science, Vol. 308(5721), pp. 534–537, 2005.

[57] D. Schurig, J. Mock, and B. Justice, Metamaterial electromagnetic cloak at microwave frequencies. Science, Vol. 314, pp. 977–980, 2006.

[58] R. Liu, C. Ji, J. Mock, J. Chin, T. Cui, and D. Smith, Broadband ground-plane cloak. Science, Vol. 323, pp. 366, 2009.

[59] W. Cai, U. Chettiar, A. Kildishev, and V. Shalaev, Optical cloaking with metamaterials. Nat. Photonics, Vol. 1, pp. 224, 2007.

[60] W. Cai, U. Chettiar, A. Kildishev, and V. Shalaev, Nonmagnetic cloak with minimized scattering. Appl. Phys. Lett., Vol. 91, pp. 111105, 2007.

[61] H. Chen, X. Jiang, and C. Chan, Extending the bandwidth of electromagnetic cloaks. Phys. Rev. B, Vol. 76, pp. 241104, 2007.

[62] H. Chen, Z. Liang, P. Yao, X. Jiang, H. Ma, and C. Chan, Extending the bandwidth of electromagnetic cloaks. Phys. Rev. B, Vol. 76, pp. 241104, 2007.

[63] H. Chen, B. Wu, B. Zhang, and J. Kong, Electromagnetic wave interactions with a metamaterial cloak. Phys. Rev. Lett., Vol. 99, pp. 063903, 2007.

[64] K. Park, B. Lee, C. Fu, and Z. Zhang, Study of the surface and bulk polaritons with a negative index metamaterial, J. Opt. Soc. Am. B, Vol. 22(5), pp. 1016-1023, 2005.

[65] C. Yan, Q. Wang, and Y. Cui, Generating mechanism of the energy-stream loops for the evanescent waves in a left-handed material slab, Optik, Vol. 121, pp. 63–67, 2010.

[66] F. Bretenaker, A. Floch, and L. Dutriaux, Direct measurement of the optical Goos–Hänchen effect in lasers, Phys. Rev. Lett., Vol. 68, pp. 931–933, 1992.

[67] H. Gilles, S. Girard, and J. Hamel, A simple measurement technique of the Goos–Hänchen effect using polarization modulation and position sensitive detector, Opt. Lett., Vol. 27, pp. 1421–1423, 2002.

[68] R. Ruppin, Surface polaritons of a left-handed material slab. J. Phys.: Condens. Matter, Vol. 13, pp. 1811–1819, 2001.

[69] V. Podolskiy and E. Narimanov, Near-sighted superlens. Opt. Lett., Vol. 30, pp. 75–77, 2005.

[70] C. Yan, Q.Wang, and Y. Cui, Generating mechanism of the energy-stream loops for the evanescent waves in a left-handed material slab. Optik, Vol. 121, pp. 63–67, 2010.

[71] C. Zhang, Z. Yuan, M. Sun, J. Wu, and P. Gao, Miniature periodic structures of left-handed materials. APPLIED OPTICS, Vol. 49, pp. 281-285, 2010.

[72] N. Skivesen, R. Horvath, and H. Pedersen, Multimode reverse-symmetry waveguide sensor for broad-range refractometry. Opt. Letters, Vol. 28, pp. 2473-2475, 2003.

[73] R. Horvath, H. Pedersen, N. Skivesen, C. Svanberg, and N. Larsen, Fabrication of reverse symmetry polymer waveguide sensor chips on nanoporous substrates using dip-floating. J. Micromech. Microeng., Vol. 15, pp. 1260–1264, 2005.

[74] N. Skivesen, R. Horvath, and H. Pedersen, Optimization of metal-clad waveguide sensors. Sens. Actuators B, Vol. 106, pp. 668-676, 2005.

[75] G. Tollin and Z. Salamon, Optical anisotropy in lipid bilayer membranes: Coupled plasmon waveguide resonance measurements of molecular orientation, polarizability, and shape. Biophys. J., Vol. 80, pp. 1557–1567, 2001.

[76] Z. Salamon, H. Macleod, and G. Tollin. Coupled plasmon-waveguide resonators: A new spectroscopic tool for probing proteolipid film structure and properties. Biophys. J., Vol. 73, pp. 2791– 2797, 1997.

[77] Z. Salamon and G. Tollin, Optical anisotropy in lipid bilayer membranes: coupled plasmon waveguide resonance measurements of molecular orientation, polarizability, and shape. Biophys. J., Vol. 80, pp. 1557–1567, 2001.

[78] Z. Salamon, D. Huang, W.A. Cramer, and G. Tollin, Coupled plasmon waveguide resonance spectroscopy studies of the cytochrome b(6)f/plastocyanin system in supported lipid bilayer membranes, Vol. 75, pp. 1874–1885, 1998.

[79] V. Podolskiyand and E. Narimanov, Near-sigheted superlens, Opt. lett., Vol. 30, pp. 75-77, 2005.

[80] P. Tien, Integrated optics and new wave phenomena in optical waveguides. Rev. Mod. Phys, Vol. 49, pp. 361–420, 1977.

[81] A. Otto and W. Sohler, Modification of the total reflection modes in a dielectric film by one metal boundary. Opt. Commun., Vol. 3, pp. 254–258, 1971.